

# Multiple Lensing of the Cosmic Microwave Background anisotropies

M. Calabrese,<sup>a</sup> C. Carbone,<sup>b,e</sup> G. Fabbian,<sup>a,f</sup> M. Baldi,<sup>c,d,e</sup> C. Baccigalupi<sup>a,f</sup>

<sup>a</sup>SISSA, Via Bonomea 256, 34136, Trieste (TS), Italy

<sup>b</sup>I.N.A.F. Osservatorio Astronomico di Brera, Via Bianchi 46, 23807, Merate (MI), Italy

<sup>c</sup>Dipartimento di Fisica e Astronomia, Alma Mater Studiorum Università di Bologna, viale Berti Pichat 6/2, I-40127, Bologna (BO), Italy

<sup>d</sup>I.N.A.F. Osservatorio Astronomico di Bologna, via Ranzani 1, I-40127 Bologna (BO), Italy

<sup>e</sup>I.N.F.N. - Sezione di Bologna, viale Berti Pichat 6/2, I-40127, Bologna (BO), Italy

<sup>f</sup>INFN, Sezione di Trieste, Via Valerio 2, I-34127 Trieste, Italy

E-mail: [mcabre@sissa.it](mailto:mcabre@sissa.it), [carmelita.carbone@brera.inaf.it](mailto:carmelita.carbone@brera.inaf.it), [gfabbian@sissa.it](mailto:gfabbian@sissa.it), [marco.baldi5@unibo.it](mailto:marco.baldi5@unibo.it), [bacci@sissa.it](mailto:bacci@sissa.it)

**Abstract.** We study the gravitational lensing effect on the Cosmic Microwave Background (CMB) anisotropies performing a ray-tracing of the primordial CMB photons through intervening large-scale structures (LSS) distribution predicted by N-Body numerical simulations with a particular focus on the precise recovery of the lens-induced polarized counterpart of the source plane. We apply both a multiple plane ray-tracing and an effective deflection approach based on the Born approximation to deflect the CMB photons trajectories through the simulated lightcone. We discuss the results obtained with both these methods together with the impact of LSS non-linear evolution on the CMB temperature and polarization power spectra. We compare our results with semi-analytical approximations implemented in Boltzmann codes like, e.g., CAMB. We show that, with our current N-body setup, the predicted lensing power is recovered with good accuracy in a wide range of multipoles while excess power with respect to semi-analytic prescriptions is observed in the lensing potential on scales  $\ell \gtrsim 3000$ . We quantify the impact of the numerical effects connected to the resolution in the N-Body simulation together with the resolution and band-limit chosen to synthesise the CMB source plane. We found these quantities to be particularly important for the simulation of B-mode polarization power spectrum.

**Keywords:** CMB - gravitational lensing - cosmology: theory - methods: numerical

---

## Contents

<b>1</b>	<b>Introduction</b>	<b>1</b>
<b>2</b>	<b>Weak lensing in Cosmology</b>	<b>3</b>
2.1	Gravitational light deflection	3
2.2	Discretised formalism	4
<b>3</b>	<b>The Algorithm</b>	<b>7</b>
3.1	Constructing mass shells	8
3.2	From shells to maps	9
3.3	Lensing the CMB	10
<b>4</b>	<b>Test and Convergence</b>	<b>11</b>
4.1	Sanity Checks	11
4.2	Lensing potential maps	11
<b>5</b>	<b>Results</b>	<b>15</b>
5.1	Numerical effects of the pixel-based methods	15
5.2	Shot-noise contribution	17
5.3	Angular power spectrum	18
<b>6</b>	<b>Discussion and Conclusions</b>	<b>23</b>
<b>A</b>	<b>Measuring angular power spectrum</b>	<b>25</b>

---

## 1 Introduction

The recent measurements of the Planck satellite [1] has unveiled a Universe well described by a cosmological model known as  $\Lambda$ CDM. In this framework, the Universe is expanding accelerated by a Dark Energy (DE) component well described by a cosmological constant  $\Lambda$ . Cold Dark Matter (CDM) is responsible for the matter halos around galaxies and galaxy clusters, while leptons and baryons take a minor part in the entire cosmic energy density budget. The robustness of the  $\Lambda$ CDM model comes primarily from advanced and enduring studies on the anisotropies in the CMB, combined with LSS and Type Ia Supernovae observations. Cosmological perturbations, scalar (such as density), vector and tensor ones can be directly observed as primary anisotropies in the CMB sky, imprinted via Compton scattering at the epoch of recombination. A step further in terms of constraining power on cosmological parameters will be achieved with the high accuracy measurements of the CMB polarization provided by the upcoming Planck polarization data and current and future high sensitivity ground-based and balloon-borne experiment like, e.g, EBEX [2], and POLARBEAR [3], SPTpol [4], ACTpol [5], Spider [6] and Keck array [7]<sup>1</sup>. These are designed to measure in particular the so-called B-modes of polarization [8, 9] which could provide a direct evidence

---

<sup>1</sup>See [http://lambda.gsfc.nasa.gov/links/experimental\\_sites.cfm](http://lambda.gsfc.nasa.gov/links/experimental_sites.cfm) for a complete list of all the latest missions and upcoming experiments

for primordial gravitational waves (tensor perturbation) generated in many inflationary scenarios [10] if such signal is detected on the degree scale. The BICEP2 collaboration recently announced a robust measurement of a signal compatible with inflationary B-modes [11] and upcoming dataset will be crucial to understand if the signal is genuinely primordial or contaminated by diffuse astrophysical polarised emission [12].

In addition to primary anisotropies previously described, the so-called secondary anisotropies [13] are imprinted in the CMB by the interaction of its photons with LSS along their paths from the last scattering surface to the observer. One of the most important sources of secondary anisotropies is the gravitational lensing effect on CMB photons by on growing matter inhomogeneities which bend and modify the geodesic path of the light. The net-effect of those deviations is a reshuffling of power in the modes of the primordial power spectrum of the total intensity and gradient-like (E-modes) component of the CMB polarization. Moreover, lensing distorts the primordial polarization patterns converting E-modes into B-modes pattern, generating power on the sub-degree scale where we expect the primordial signal to be negligible (for a complete review, see [14]). The progress towards the detection of lensing in the CMB data has been slow, since measurements of the CMB precise enough to enable a detection of weak lensing were not available until recently. Moreover, picking out non-Gaussian signatures - which arise from mode mixing on different scales induced by lensing - in the measured CMB sky by itself is extremely difficult, due to confusion from systematics, foregrounds, and limited angular resolution. The first robust detections of the lensing effect were done using temperature data only by ACT [15] and SPT [16, 17], and later confirmed by Planck with a significance greater than  $25\sigma$ . Only recently, however, the evidence of lensing was detected for the first time in polarization data by POLARBEAR [18, 19] and SPTpol [20].

The interest on CMB lensing for cosmological application lies in the possibility of extracting information about the projected large scale structure potential, and thus to constrain the late time evolution of the Universe and, e.g. the Dark Energy and massive neutrinos properties [14, 21–23]. A step forward to probe DE would be to cross correlate the CMB lensing with the observations of the actual lenses in LSS surveys as seen by independent tracers of the matter distribution. This option has already been exploited to obtained astrophysical and cosmological information by, e.g., SPT, ACT and, more recently, by POLARBEAR collaborations [20, 24–27], but a major improvement is expected in about a decade with the observations of the ESA-Euclid satellite. This will combine arc-second imaging of billions of galaxies with photometric redshift accuracy corresponding to the percent level, between redshifts  $0 \lesssim z \lesssim 2$  [28, 29]. To fully exploit the capabilities of these cross correlation studies [30], accurate prediction for the common observables are crucial.

The most accurate way to obtain predictions for observables of weak-lensing surveys is to perform ray-tracing through large, high resolution N-Body numerical simulations to study the full non-linear and hierarchical growth of cosmic structures. Although this approaches are computationally very demanding, they allow to check and balance the approximations and assumptions made in widely-used semi-analytic models, adjusting and extending these models if necessary. Numerous ray-tracing methods have been developed so far in the context of both strong and weak gravitational lensing. Though exact algorithm are available [31], they are not suitable for application targeting observations of large fraction of the sky for computational reasons. A simpler and popular approach consists in using the matter distribution in the N-body simulations to calculate lensing observables by photon ray-tracing along “unperturbed”, i. e. undeflected light paths in the so-called Born approximation (e.g.

[32–34]). In particular, [35] applied this technique to study a set of N-Body simulation with different cosmologies and DE dynamics, to investigate the variation of the lensing pattern with respect to the standard  $\Lambda$ CDM model. [36], conversely, showed that the correct integrated matter distribution used to lens incoming CMB photons in the Born approximation can be properly reconstructed using standard lensing reconstruction techniques [37]. However, when facing a complex cosmological structure, we must take into account that each light ray undergoes several distortions due to matter inhomogeneities, i.e. approximating the actual path of a photon instead of adopting a single effective deviation from the unperturbed, line-of-sight integral assumed in Born approximation. The single effective lens must therefore be replaced by a multiple-lens (ML) approach, where large volumes of matter are projected onto a series of lens planes [38–42] so that the continuous deflection experienced by a light ray is approximated by finite deflections at each of the planes. A ML algorithm full-sky CMB lensing application was sketched in [43] who simulated lensed CMB maps in temperature only with an angular resolution of  $0.9'$ . However detailed comparison of the effective Born approximation method and the ML approach was not discussed and only the results derived in the Born approximation scenario were presented.

In this work, we implemented a multiple plane ray-tracing algorithm to lens CMB temperature and polarization fields combining the aforementioned work by [43] and using the lightcone reconstruction from a single N-Body simulation of [44]. The final rationale will be to investigate DE effects in different cosmologies at arc-minutes scales, where are expected to be most noticeable. At these scales, the Born approximation is likely expected not to trace with high accuracy local deviations due to small-scales inhomogeneities, and thus a more precise and realistic method is needed. Moreover, in order to be successful, we need to be able to control and discriminate between physical non-linearities of the N-Body simulations from numerical issues connected to the various approximations in both the lensing algorithm and the simulation itself. A detailed analysis of these issues together with their impact on the lensed CMB observables will thus be presented. The present paper is intended to be the first one of a series investigating the response of CMB lensing upon DE and/or modified gravity cosmologies or neutrino physics, as well as the feasibility and the constraining power of cross-correlation studies involving Planck and simulated Euclid data. This paper is organized as follows: in the Section 2, we introduce the theoretical background and notation used for our lensing algorithm. In Section 3 we discuss our ray-tracing technique, which is then tested and evaluated in Section 4. Section 5 shows results for the lensed temperature and polarization fields of the CMB, with particular emphasis on differences and similarities between the Born approximation and the multiple-lens approach. The last Section draws the conclusions.

## 2 Weak lensing in Cosmology

### 2.1 Gravitational light deflection

In this Section, we briefly recall the definition of the relevant quantities concerning the weak lensing effect that will be used in the rest of the paper. We refer the reader to more specialised reviews for a general treatment of the weak lensing effect [14, 45]. Following the approach in [43], we assume a coordinate system based on physical time  $t$ , two angular coordinates  $\theta = (\theta_1, \theta_2)$ , and the line-of-sight, radial comoving distance  $\eta$  relative to the observer. In a standard Universe with a weakly perturbed Friedmann-Lemaître-Robertson-Walker (FLRW)

metric, a light ray approaching a matter density distribution is deviated by an angle

$$d\alpha = -2\nabla_{\perp}\Psi d\eta, \quad (2.1)$$

where  $d\alpha$  is called deflection angle,  $\Psi$  is the Newtonian potential and  $\nabla_{\perp}$  denotes the spatial gradient on a plane perpendicular to the light propagation direction. The gradient in Eq. (2.1) is defined in the small-angle limit as  $\nabla_{\perp} = (\partial/\partial\theta_1, \partial/\partial\theta_2)$  where  $(\theta_1, \theta_2)$  describe a coordinate system orthogonal to the light ray trajectory. The transverse shift of the light ray position at  $\eta$  due to a deflection at  $\eta'$  can be thus written as

$$d\mathbf{x}(\eta) = D_A(\eta - \eta')d\alpha(\eta'), \quad (2.2)$$

where  $D_A(\eta)$  is the comoving angular diameter distance. In weak lensing calculations, an “effective” approach is commonly used, where the effect of deflectors along the entire line of sight is approximated by a projected potential computed along a fiducial un-deflected ray (Born approximation). The final angular position  $\boldsymbol{\theta}(\eta) = \mathbf{x}(\eta)/D_A(\eta)$  is therefore given by

$$\begin{aligned} \boldsymbol{\theta}(\eta) &= \boldsymbol{\theta}(0) - \frac{2}{D_A(\eta)} \int_0^{\eta} d\eta' D_A(\eta - \eta') \nabla_{\perp} \Psi = \\ &= \boldsymbol{\theta}(0) + \tilde{\boldsymbol{\alpha}}(\eta), \end{aligned} \quad (2.3)$$

where  $\tilde{\boldsymbol{\alpha}}$  is the total effective deflection from the initial angular position of the light ray at the observer position  $\boldsymbol{\theta}(\eta = 0)$ . Note that the integral in Eq. (2.3) is evaluated along the light ray trajectory and is thus an implicit equation for  $\boldsymbol{\theta}(\eta)$ . It is convenient to define  $\tilde{\boldsymbol{\alpha}}$  as the gradient of an effective potential including the contributions to the final deviation of all the structures present between the observer and the background source plane located at a comoving distance  $\eta_s$ , i.e.  $\tilde{\boldsymbol{\alpha}} = -\nabla_{\perp}\psi^{eff}$ , where

$$\psi^{eff}(\boldsymbol{\theta}) = \frac{2}{D_A(\eta_s)} \int_0^{\eta_s} d\eta \frac{D_A(\eta_s - \eta)}{D_A(\eta)} \Psi(\boldsymbol{\theta}, \eta). \quad (2.4)$$

The latter quantity is commonly known as the lensing potential. If we consider in particular the case of the weak lensing of CMB anisotropies,  $\eta_s$  is the comoving distance to the last scattering surface. An effective convergence field can be also defined in a similar manner:

$$\kappa(\boldsymbol{\theta}) \equiv \frac{1}{2} \nabla_{\perp}^2 \psi^{eff}(\boldsymbol{\theta}) = \frac{2}{D_A(\eta_s)} \int_0^{\eta_s} d\eta \frac{D_A(\eta_s - \eta)}{D_A(\eta)} \nabla_{\perp}^2 \Psi(\boldsymbol{\theta}, \eta). \quad (2.5)$$

## 2.2 Discretised formalism

The previous set of equations can be discretised by dividing the interval between the observer and the source into  $N$  concentric shells, each of comoving thickness  $\Delta\eta$ . The matter in the  $k$ -th shell is projected onto a spherical, two-dimensional sheet which is positioned in the middle of the two edges of the matter shell<sup>2</sup>, at comoving distance  $\eta_k$ . To simplify the following calculations, it is common practice to use angular differential operators defined on the sphere instead of spatial ones, since we will be working with 2D spherical projections of the matter distribution. We thus can rewrite Eq. (2.1) in terms of the angular gradient  $\nabla_{\hat{\mathbf{n}}}$  as

$$d\alpha = -\frac{2}{D_A(\eta)} \nabla_{\hat{\mathbf{n}}} \Psi d\eta. \quad (2.6)$$

---

<sup>2</sup>The shell index  $k$  increases as moving away from the source plane.

Note that the versor  $\hat{\mathbf{n}}$  refers to angular coordinates on the sphere, or  $\boldsymbol{\theta} = \eta\hat{\mathbf{n}}$ . A photon in the  $k$ -th shell at  $\eta_k$  is deflected - due to the presence of matter - by an angle  $\boldsymbol{\alpha}^{(k)}$  which can be approximated by

$$\begin{aligned}\boldsymbol{\alpha}^{(k)}(\hat{\mathbf{n}}) &= -\frac{2}{D_A(\eta_k)} \frac{D_A(\eta_s - \eta_k)}{D_A(\eta_s)} \int_{\eta_k - \Delta\eta/2}^{\eta_k + \Delta\eta/2} \nabla_{\hat{\mathbf{n}}} \Psi(\tilde{\eta}\hat{\mathbf{n}}; \tilde{\eta}) d\tilde{\eta}, \\ &= -\nabla_{\hat{\mathbf{n}}} \psi^{(k)}(\hat{\mathbf{n}}),\end{aligned}\tag{2.7}$$

where the 2-D gravitational potential on the sphere is defined as

$$\Phi^{(k)}(\hat{\mathbf{n}}) = \frac{2}{D_A(\eta_k)} \int_{\eta_k - \Delta\eta/2}^{\eta_k + \Delta\eta/2} \Psi(\tilde{\eta}\hat{\mathbf{n}}; \tilde{\eta}) d\tilde{\eta},\tag{2.8}$$

and the corresponding contribution to the lensing potential is given by

$$\psi^{(k)}(\hat{\mathbf{n}}) = \frac{D_A(\eta_s - \eta_k)}{D_A(\eta_s)} \Phi^{(k)}(\hat{\mathbf{n}}).\tag{2.9}$$

In the previous equations, the notation  $(\eta\hat{\mathbf{n}}; \eta)$  indicates that the potential is evaluated when the photon is at the position  $\eta\hat{\mathbf{n}}$  on the sky, at the comoving distance  $\eta$  from the observer. We can relate the gravitational potential to the mass overdensity in the shell using the Poisson equation

$$\nabla^2 \Psi = \frac{4\pi G}{c^2} \frac{\rho - \bar{\rho}}{(1+z)^2},\tag{2.10}$$

where  $\bar{\rho}$  is the mean matter density of the Universe at redshift  $z$ . As in [46], we can integrate the above equation along the line of sight to obtain the two dimensional version of the Poisson equation for the  $k$ -th mass shell:

$$\nabla_{\hat{\mathbf{n}}}^2 \Phi^{(k)}(\hat{\mathbf{n}}) = \frac{8\pi G}{c^2} \frac{D_A(\eta_k)}{(1+z_k)^2} \Delta_{\Sigma}^{(k)}(\hat{\mathbf{n}}),\tag{2.11}$$

where the surface mass density is defined as

$$\Delta_{\Sigma}^{(k)}(\hat{\mathbf{n}}) = \int_{\eta_k - \Delta\eta/2}^{\eta_k + \Delta\eta/2} (\rho - \bar{\rho}) d\tilde{\eta}.\tag{2.12}$$

In Eq (2.11) we have dropped the term containing the derivatives in the radial direction, ignoring thus long wavelength fluctuations along the line-of-sight via the Limber approximation [39]. However, as argued by [42, 43], this is, at best, an approximation. In particular [47] showed that this assumption neglects extra terms that become non-zero in presence of realistic finite width lens plane. The problem arises because the matter distribution and, thus, the potential itself may become discontinuous at the boundaries if periodic conditions are not enforced. Nevertheless, these corrections to the lens-plane approach adopting the Born approximation which has been used for this work (see Sect. 3) confine this problem to the single shells. In fact, partial derivatives in the transverse plane commute with the integral evaluated along the whole line of sight, resulting in the cancellation of line-of-sight modes as required in the Limber approximation of the integral. <sup>3</sup>

---

<sup>3</sup>Note for example that assuming a flat-sky approximation, unlike what has been done in this work, is a stronger assumption with respect to the Limber approximation and results in a well-known excess of power on large scales as seen, e.g., by [48].

We use the following definition for the convergence field  $K^{(k)}$  at the  $k$ -th shell,

$$K^{(k)}(\hat{\mathbf{n}}) = \frac{4\pi G}{c^2} \frac{D_A(\eta_k)}{(1+z_k)^2} \Delta_\Sigma^{(k)}(\hat{\mathbf{n}}), \quad (2.13)$$

to rewrite Eq. (2.11) as

$$\nabla_{\hat{\mathbf{n}}}^2 \Phi^{(k)}(\hat{\mathbf{n}}) = 2K^{(k)}(\hat{\mathbf{n}}). \quad (2.14)$$

The lensing potential on the sphere is related to  $K$  via Eq. (2.14), and it can be easily computed by expanding both sides of the Poisson equation in spherical harmonics, obtaining the following algebraic relation between the harmonic coefficients of the two fields:

$$\Phi_{\ell m} = \frac{2}{\ell(\ell+1)} K_{\ell m}. \quad (2.15)$$

The monopole term in the lensing potential does not contribute to the deflection field: therefore to avoid any divergence in the above equation we can safely set to zero  $\Phi_{\ell m}$  for  $\ell = 0$  in all calculations. The quantity  $K$  is directly computed when the matter distribution in the shell is radially projected onto the spherical map; as discussed in Sect. 3.2, it is useful to define an angular surface mass density  $\Delta_\Sigma^\theta(\hat{\mathbf{n}})$  as the mass per steradians,

$$\Delta_\Sigma^{\theta(k)}(\hat{\mathbf{n}}) = \int_{\eta_k - \Delta\eta/2}^{\eta_k + \Delta\eta/2} (\rho - \bar{\rho}) \frac{D_A(\tilde{\eta})^2}{(1+\tilde{z})^3} d\tilde{\eta}. \quad (2.16)$$

such that Eq. (2.13) can be rewritten as:

$$K^{(k)}(\hat{\mathbf{n}}) = \frac{4\pi G}{c^2} \frac{1+z_k}{D_A(\eta_k)} \Delta_\Sigma^{\theta(k)}(\hat{\mathbf{n}}). \quad (2.17)$$

Finally, the vector field  $\boldsymbol{\alpha}(\hat{\mathbf{n}})$  will be synthesised, as described in [8, 9], from the spherical harmonic components of the potential in terms of spin-1 spherical harmonics. The multiple-plane lens formalism can be also applied to exploit the effective or single-plane approximation to lens the CMB. Eqs. (2.4) and (2.5) can be discretised into the following sums,

$$\psi^{\text{eff}}(\hat{\mathbf{n}}) = \sum_j \frac{D_A(\eta_s - \eta_j)}{D_A(\eta_s)} \Phi^{(j)}, \quad (2.18)$$

$$\kappa(\hat{\mathbf{n}}) = \sum_j \frac{D_A(\eta_s - \eta_j)}{D_A(\eta_s)} K^{(j)}, \quad (2.19)$$

where we used the previous definitions of quantities on the  $j$ -th lens. In the same framework, the convergence  $\kappa$  can be seen as just a weighted projected surface density [41, 44]:

$$\kappa(\boldsymbol{\theta}) = \frac{3H_0^2 \Omega_{m,0}}{2c^2} \int d\eta \delta(\eta, \boldsymbol{\theta}) \frac{D_A(\eta_s - \eta) D_A(\eta)}{D_A(\eta_s) a(\eta)}, \quad (2.20)$$

where  $\delta$  is the 3D matter density at radial distance  $\eta$  and angular position  $\boldsymbol{\theta}$ ,  $D_A(\eta_s)$  is the position of the lensing source at the last scattering surface and  $a(\eta)$  is the scale factor at  $\eta$ . Based on the definition in Eq. (2.20), the angular power spectrum of the convergence becomes

$$C_\ell^{\kappa\kappa} = \frac{9H_0^4 \Omega_{m,0}^2}{4c^4} \int_0^{\eta_s} d\eta P(k, z) \left( \frac{D_A(\eta_s - \eta)}{D_A(\eta_s) a} \right)^2, \quad (2.21)$$



where  $P(k, z)$  is 3D matter power spectrum, computed via the Limber approximation at  $k = \ell/D_A(\eta(z))$ , valid for  $\ell > 10$  within a few percent accuracy [46]. The discretised equation reads:

$$C_\ell^{\kappa\kappa} = \frac{9H_0^4\Omega_{m,0}^2}{4c^4} \sum_k \Delta\eta P(\ell/D_A(\eta_k), z_k) \left( \frac{D_A(\eta_s - \eta_k)}{D_A(\eta_s)a_k} \right)^2, \quad (2.22)$$

summing all over the  $k$  lens plane. Note that the convergence field can be converted into lensing potential using the Poisson equation, or in terms of the angular power spectrum:

$$C_\ell^{\psi\psi} = \frac{4}{\ell^2(\ell+1)^2} C_\ell^{\kappa\kappa}. \quad (2.23)$$

### 3 The Algorithm

In the previous Section we have described the basic formalism and equations to evaluate the weak lensing effects on the full sky. In this Section we proceed outlining the basic steps of the algorithm used to lens the CMB photons throughout:

- (i) starting from an N-Body simulation, we create 3D simulated matter distribution around a chosen observer;
- (ii) taking advantage of the proper sampling in redshift of the simulation, we select different shells of matter at different times to reconstruct our past lightcone and mimic cosmological evolution;
- (iii) we project all the matter in a given shell over a single 2D spherical map which acts as lensing plane;
- (iv) we solve the full-sky Poisson equation in the harmonic domain and compute the lensing potential map for the single lens plane and for the integrated potential of Eq. 2.18;
- (v) we use this lensing potential map to lens the CMB source plane;
- (vi) we repeat step (iii)-(v) for all the selected shells, thus following the evolution of the source plane

In our analysis we have used a N-Body simulation of cosmic structure formation in a flat  $\Lambda$ CDM universe with an underlying cosmology described by the following set of cosmological parameters:

$$\{\Omega_{dm}, \Omega_b, \Omega_\Lambda, n_s, \sigma_8, H_0\} = \{0.226, 0.0451, 0.729, 0.966, 0.809, 70.3 \text{ Km/s/Mpc}\}.$$

The simulation follows the evolution of the matter distribution in a cubic (comoving) volume  $(1000 h^{-1}\text{Mpc})^3$  from redshift  $z = 10$  to present time using a modified TreePM version of GADGET<sup>4</sup>, specifically developed to include all the additional physical effects that characterize different dark energy models (see [49] for a detailed description of the code). The whole numerical project goes under the name of COupled Dark Energy Cosmological Simulation, or CoDECS<sup>5</sup>. At present, they include two distinct set of publicly available runs, the L-CoDECS and the H-CoDECS. The L-CoDECS simulations consist in  $1024^3$  CDM and  $1024^3$

<sup>4</sup><http://www.mpa-garching.mpg.de/gadget>

<sup>5</sup>[www.marcobaldi.it/CoDECS](http://www.marcobaldi.it/CoDECS)



baryon particles, both treated with collisionless dynamics only, which means that baryonic particles are not considered as gas particles but just as a different family of collisionless particles distinguished from CDM. This is done in order to account for the effect of the uncoupled baryon fraction in cDE models which would not be correctly represented by CDM-only simulations. The mass resolution at  $z = 0$  for this set of simulations is  $M_{CDM} = 5.84 \times 10^{10} M_{\odot}/h$  for CDM and  $M_b = 1.17 \times 10^{10} M_{\odot}/h$  for baryons, while the gravitational softening is set to  $\epsilon_s = 20$  comoving  $kpc/h$ , corresponding to 0.04 times the mean linear inter-particle separation. The H-CoDECS simulations are instead adiabatic hydrodynamical simulations on much smaller scales, which we do not consider in the present work. In this paper we will analyse only the  $\Lambda$ CDM simulation of the L-CoDECS suite, while the analysis on different DE models will be discussed in a future paper.

### 3.1 Constructing mass shells

N-Body simulations are usually stored as a series of snapshots, each representing the simulation box at a certain stage of its evolution. As a first step, we fix the observer. We consider the last snapshot, at redshift  $z = 0$ , and compute the center of mass of the whole simulation. This centre represents the origin of our new system of reference, which sees all the CMB radiation around it. As we explore the universe around the new origin, the further we move in space, the more we look back in time and see how structures develop and grow, until we reach a volume large enough to carry out the integration for CMB lensing. One of the difficulties in this approach is that, even though the size of the simulation box is limited, we need to use the box to reconstruct the full backwards lightcone. Therefore, we need to replicate the box volume several times in space, so that the entire observable volume is covered. In particular, as described in [50], the simulation volume needs to be repeated along both the positive and negative directions of the three principal Cartesian axes  $x$ ,  $y$ , and  $z$ , keeping the origin centered on the observer.

To construct the all-sky past light cone we exploit the simulation outputs at different times which are equally spaced in the logarithm of the scale factor,  $\log_{10}(a)$ , corresponding to an average spacing of  $150 \text{ Mpc} h^{-1}$  comoving. The need to repeat the simulation volume due to its finite size immediately means that, without augmenting large-scale structures, the maps will suffer from a deficit of lensing power on large angular scales, due to the finite box size. More importantly, a scheme is required to avoid the repetition of the same structures along the line of sight. Previous studies that constructed simulated lightcone maps for small patches of the sky typically simply randomized each of the repeated boxes along the past lightcone by applying independent random translations and reflections (e.g. [51]). However, in the present application this procedure would produce artifacts like ripples in the simulated deflection-angle field, because the gravitational field would become discontinuous at box boundaries, leading to jumps in the deflection angle. It is therefore mandatory that the simulated lensing potential of our all sky maps is everywhere continuous on the sky, which requires that the 3D tessellation of the peculiar gravitational potential is continuous transverse to every line of sight.

Following [34, 50], our solution is to divide up the volume out to the redshift covered by the simulation  $z_{max}$  into larger spherical shells, each of thickness  $1 \text{ Gpc} h^{-1}$  comoving (as the box size). All the simulation boxes falling into the same larger shell are made to undergo the same, coherent randomization process, i.e. they are all translated and rotated with the same random vectors generating a homogeneous coordinate transformation throughout the shell. But this randomization changes from shell to shell.

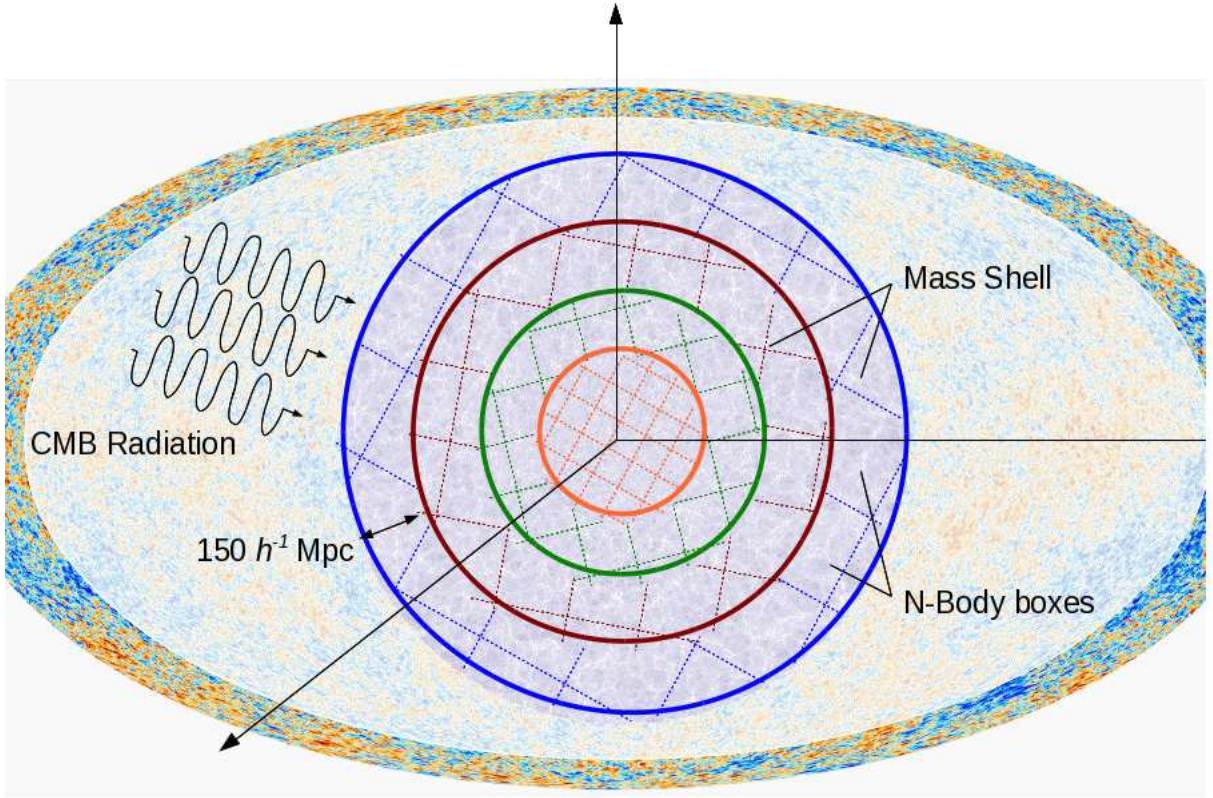


**Figure 1:** Sketch of the adopted stacking process. The crossing of CMB photons through the dark matter distribution of the Universe is followed by stacking and replicating the boxes of the N-Body simulation to fill the entire shell volume. Each shell has a thickness of  $\sim 150h^{-1}$  Mpc (comoving).

Figure 1 shows a schematic sketch of this stacking technique. As already mentioned, the need to repeat the simulation volume due to its finite size implies that the maps will suffer from a non proper description of the large angular scales. We note however that if the box size is sufficiently big like in e.g. [52] this procedure is no longer necessary, at least up to the redshift covered by the simulation size. The final results of the whole process is a series of concentric shells that substitutes our snapshots. For our specific input N-body simulation, we get 25 matter shells, building a lightcone spanning from  $z = 0$  to  $z_{max} = 10$ .

### 3.2 From shells to maps

Following the scheme proposed in [43], we convert the position of a particle distributed within a 3D matter shell into its angular position on the 2D spherical map of the (projected) surface matter density. Note that among all the particles in the simulation, only the ones falling within the radii of the spherical shell of width  $150 \text{ Mpc} h^{-1}$  are projected onto the 2D spherical

map. We then assign each particle to a specific sky pixel in the HEALPix<sup>6</sup> pixelisation scheme starting from its spherical coordinates  $(\theta, \phi)$  and using the `ang2pix` routine of the HEALPix suite. We place the particle mass into the pixel so that each sky pixel reads  $\Sigma_p^\theta = m_p/\Omega_{pix}$ , where  $\Omega_{pix}$  is the area of a pixel in steradians. If  $n$  particles fall inside the beam defined by a pixel, the pixel will have a surface mass density of  $n\Sigma_p^\theta$ . In HEALPix, the resolution is controlled by the parameter `NSIDE` which determines the number  $N_{pix}$  of pixels of equal area into which the entire sphere is divided through the relation  $N_{pix} = 12 \times \text{NSIDE}^2$ , so that each pixel has an area of  $\Omega_{pix} = 4\pi/N_{pix}$  sterad. The angular resolution is often expressed through the number  $\theta_{res} = \sqrt{\Omega_{pix}}$ . For a value of `NSIDE` set to 2048 (4096), the corresponding an angular resolution is  $1'.717$  ( $0'.858$ ).

The real interesting quantity in our lensing calculation, in addition to the surface mass density, is the convergence map  $K^{(k)}(\hat{\mathbf{n}})$  on the lens-plane  $k$ . To get this quantity we first compute the overdensity maps  $(\Delta\Sigma^\theta)$  using the average surface mass density of the 2D map. Then we multiply by this map by its geometrical weight  $(1+z_k)/D_A(\eta_k)$ , depending on the lens plane distance from the observer and its redshift, assumed to be an average between the time at the beginning and the end of the shell (see Eq. 2.17). As a final step, we produce a convergence map from each shell of the lightcone which will become our lensing planes to lens the CMB signal.

From the convergence map  $K^{(k)}(\hat{\mathbf{n}})$  we then extract the gravitational potential  $\psi^{(k)}$  following Eq. (2.15), using the HEALPix spherical harmonics transform (SHT) routines to decompose  $K^{(k)}(\hat{\mathbf{n}})$  into its harmonic coefficients  $K_{\ell m}$ . Note that we correct the smoothing of the true underlying continuous field on the pixel scale directly in the harmonic domain when we solve for the Poisson equation (see Appendix A for more details).

### 3.3 Lensing the CMB

To propagate the CMB photons through the different shells we adopt a pixel-based approach first presented in [53]. Starting from the  $\psi_{\ell m}$  coefficients, we compute the deflection field for each shell  $\alpha^{(k)}$  evaluating Eq. (2.7) in the harmonic domain. Being the deflection field purely a gradient field (i.e. a spin-1 curl-free vector field), it can be easily evaluated with a spin-1 SHT. The E and B decomposition of the field reads:

$${}_1\alpha_{\ell m}^E{}^{(k)} = \sqrt{\ell(\ell+1)}\psi_{\ell m}^{(k)} \quad {}_1\alpha_{\ell m}^B{}^{(k)} = 0. \quad (3.1)$$

Once the deflection field is give, each pixel-based method remaps the CMB field as a function of the position on the sky assuming the lensed signal observed along a direction  $\hat{\mathbf{n}}$  equal to the signal coming from another direction  $\hat{\mathbf{n}}'$ ,

$$\hat{\mathbf{n}}'^{(k)} = \hat{\mathbf{n}}^{(k-1)} + \alpha^{(k)}, \quad (3.2)$$

where  $\hat{\mathbf{n}}^{(k-1)}$  represents the unlensed position of the CMB photons at the previous step. To our level of approximation  $\|\nabla\Phi\|$  is assumed to be constant between  $\hat{\mathbf{n}}^{(k-1)}$  and  $\hat{\mathbf{n}}'^{(k)}$ , consistent with working out the lensing potential in the Born approximation between two consecutive shells. In this work we adopted the publicly available code `LensPix` to propagate the CMB signal through all the lensing shells. `LensPix` implements a pixel-based lensing method using a bi-cubic polynomial interpolation scheme to evaluate the source plane along the displaced direction. This method has been shown to be accurate at the sub-percent level

---

<sup>6</sup><http://healpix.sourceforge.net>

to produce temperature and E-modes signal. However, the recovery of the B-modes of the CMB polarization is more difficult because B-modes are more sensitive to numerical effects like the involved resolution and the choice of the band-limit (i.e. the power cut-off  $\ell_{max}$ ) in the calculation. We will discuss the impact on the relevant numerical effects in Section 5.1 and we refer the reader to [54] for a complete discussion of the numerical problems and accuracy of pixel based methods.

Finally, note that the simulated lightcone recovers the distribution of matter in the Universe up to  $z_{max} = 10$ , and therefore the primordial CMB fields are lensed by LSS only in this specific redshift interval. In other words, photons are ray-traced in a Universe evolving from  $z_{max}$  to  $z = 0$ . The impact of high-redshifts contributions is besides the goal of this algorithm, which will be tested against analytical and semi-analytical computations which we have modified accordingly to perform CMB lensing only in this redshift range.

## 4 Test and Convergence

### 4.1 Sanity Checks

In this section we assess the reliability of our code by performing sanity checks similarly to [43] to ensure that all the steps of the algorithm give stable and robust results. For the first test, we show that the total mass selected in each 3D matter slice is equal to the theoretical mass expected from the assumed cosmological model in the simulation, given by

$$M_{slice}^{theory} = 4\pi\Omega_{m,0}\rho_c\bar{\eta}^2\Delta\eta, \quad (4.1)$$

where  $\Delta\eta$  is the comoving thickness of the slice at a comoving (average) distance  $\eta$ ,  $\rho_c$  is the critical density and  $\Omega_{m,0}$  corresponds to the present value of the matter density parameter. We compare this quantity with the total mass obtained from the surface density maps ( $\Sigma^\theta$ ) drawn with our procedure,

$$M_{slice} = \sum_{p=1}^{N_{pix}} \Sigma_p^\theta \Omega_{pix}, \quad (4.2)$$

by summing on all pixels of the spherical map. Figure 2 shows the fractional difference between the two masses for the different redshifts at which each spherical map is located. The agreement is very good within a few percents. As similarly found by [43], fluctuations respect to the theory appear at low  $z$ , due to the tension between the small comoving volume as seen by the observer, and a highly-clustered matter distribution at late times. Including or excluding large dark matter halos in the selection process therefore leads to differences between the mass extracted from the maps and the theoretical one.

As a second test, we make sure that the projection from the simulation box onto the map has been properly performed. Figure 3 displays the probability density function (PDF) as recovered from the surface mass density maps, compared with analytic PDFs, drawn from the data, such as the Gaussian and log-normal ones (as in [55, 56]). The extracted PDFs are quite similar to the ones found by [43], even if - as already observed by the same authors - the analytical PDFs could not fit well the data especially at high surface mass density where the non-linearities becomes important and where accurate models are yet unknown.

### 4.2 Lensing potential maps

Once surface density maps have been validated, we can move one step forward and verify lensing quantities. As described in Section 2.2, the effective convergence plane is computed

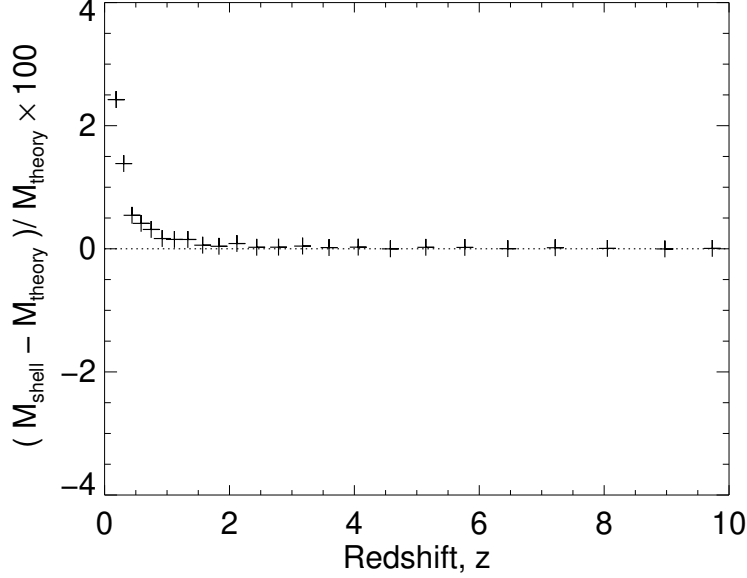


**Figure 2:** The total mass for each shell compared with the one expected from theory (fractional difference) as function of redshift.

by weighting the surface mass density planes with appropriate geometrical factors. We validated such convergence maps by comparing the extracted power spectra to the theoretical expectations based on semi-analytical computations of the matter perturbation evolution as implemented in the publicly available Boltzmann code `CAMB`<sup>7</sup>. Adopting the Born approximation, we drew an “effective” convergence map, as described in Eq. (2.5), using the matter shells at different redshifts. We then compute, in Limber approximation of Eq. (2.21), the theoretical convergence angular power spectrum, exploiting directly the 3D matter power spectrum computed with `CAMB`. The comparison between the simulated and the analytical power spectra is shown in Figure 4. In both cases we perform the integration up to a specific redshift  $z^*$  to assess the validity of the maps at different times. We observe that the measured spectra agree at high accuracy with the theoretical predictions on a large interval of angular scales, indicating the validity of our map-making procedure. As expected, the lack of power at small multipoles  $\ell \lesssim 50$  is due to the finite box size of the N-Body simulation. A source of possible contamination of the signal is the so-called *shot-noise*, due to the finite particle density in the N-Body simulation. The shot-noise power spectrum can be computed analytically substituting the shot noise power spectrum  $P^{Shot}(k, z) = 1/\bar{n}_k$  in Eq. (2.22), where  $\bar{n}_k = N_k / (4\pi\eta_k^2\Delta\eta)$  and  $N_k$  is the total number of particles in the  $k$ -th shell, we obtain the shot-noise contribution to the convergence:

$$C_{\ell}^{\kappa\kappa, Shot} = \frac{9H_0^4\Omega_{m,0}^2}{4c^4} \sum_k \Delta\eta \frac{1}{\bar{n}_k} \left( \frac{D_A(\eta_s - \eta_k)}{D_A(\eta_s)a_k} \right)^2. \quad (4.3)$$

---

<sup>7</sup><http://camb.info>



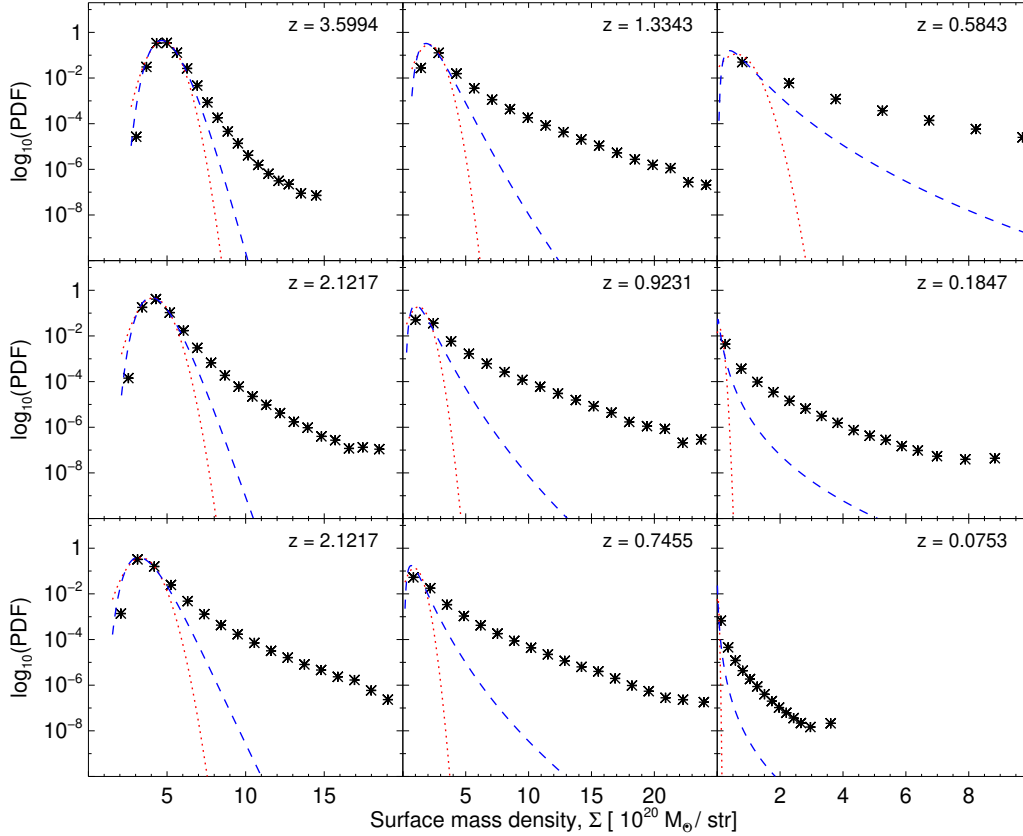


**Figure 3:** The probability density function (PDF) of the surface mass density in the lensing-planes (crosses) compared with the Gaussian (red, dotted line) and the log-normal (blue, dashed line).

For the N-body simulation used in this code the shot-noise is small at all redshifts given the high spatial resolution and high number of particles employed (see Figure 4). Figure 5 shows a comparison of the partial contributions to lensing potential angular power spectrum computed at different redshifts with the corresponding analytical signal given by Eqs. (2.22) and (2.23) in which we insert the 3D matter power spectrum extracted from CAMB. In this case, the label  $z$  refers to the redshift of the matter spherical map which contributes to the lensing potential at that time. Each power spectrum represents the “real” map given as input to `LensPix` in order to obtain the final CMB lensed maps in the multiple plane approach. Here the Limber approximation is necessary to solve the Poisson equation using the transverse part of the Laplacian only, thus neglecting line-of-sight contributions as previously discussed in Sec. 2.2. The agreement between simulated and analytical  $C_\ell^{\psi\psi}$  as a function of the redshift is clearly observable from Figure 5. The recovered signal is stable and coherent on a whole range of multipoles. As discussed in the following, we assume a very conservative choice for the map resolution and power cut-off  $\ell_{max}$  ( $NSIDE = \ell_{max} = 4096$ ). Therefore, we do not expect this result to be affected by power aliasing given that an HEALPix grid with resolution set by `NSIDE` parameter should be able to properly sample modes up to  $\ell \approx 2 \times NSIDE$ . An interesting and comprehensive way to see how the lensing process behaves at different scales

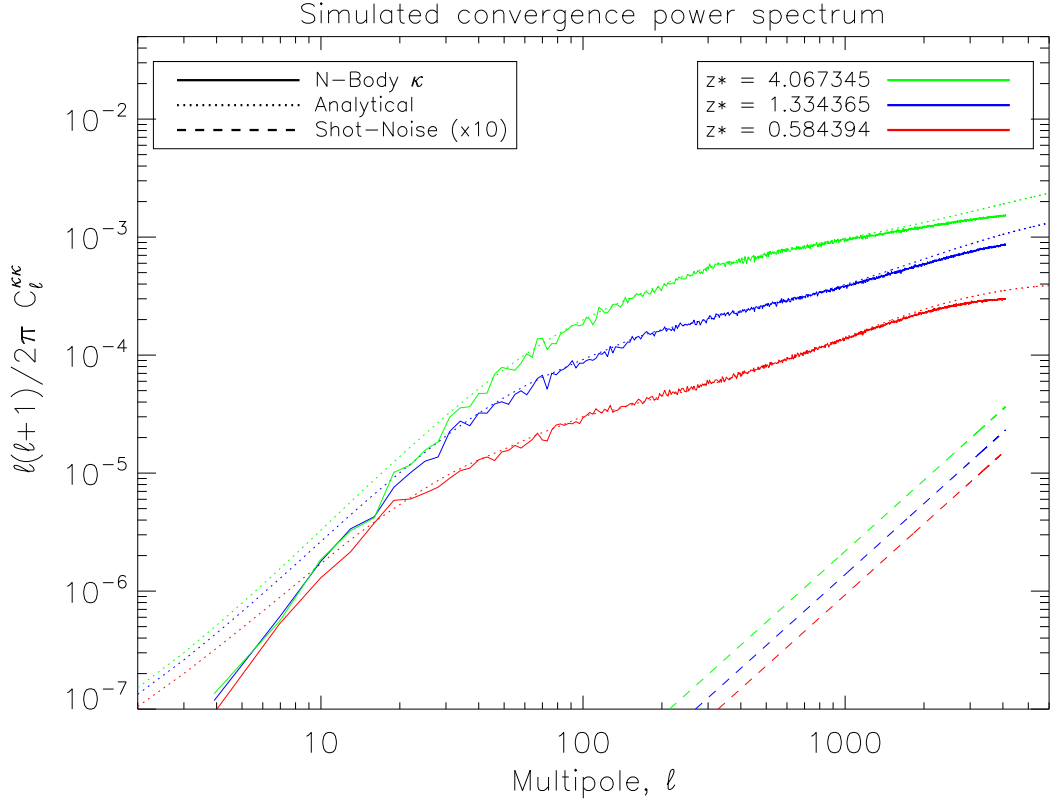


**Figure 4:** Angular power spectrum from the “effective” convergence map (solid lines) compared with theory predictions (dotted line) at three different redshifts,  $z^* \simeq 0.6, 1.3, 4$ . Dashed lines quantify the shot-noise contribution for each maps. Note that the shot-noise power spectra is multiplied by a factor of 10 for visualization purposes.

is to look at the integrated potential, as computed in Born approximation using Eq. (2.18). In Figure 6 we show the angular power spectrum for the effective lensing potential and its shot-noise contribution, compared to the semi-analytical realizations by CAMB, where we fix the maximum redshift of the integration,  $z_{max}$ , to be the same as the maximum redshift used in our map-making procedure. Also in this case, we find a very good agreement between the two methods, within the  $1\sigma$  uncertainty for the semi-analytical spectrum. As in Figures 4 and 5 the spectrum shows a lack of power due to the finite size of the simulation box for  $\ell < 50$ . Note that the shot-noise contribution is negligible, as we have multiplied it by a factor of 10 such that it could be compared with the lensing potential signal. In general, at intermediate scales our spectra show a small deficit of power, within 3% with respect to the HALOFIT prescription [57], while at small scales, even after the shot-noise subtraction (blue lines), the signal seems to increase towards  $\ell \approx 3500$ , likely due to the underlying non-linear clustering underestimated by the analytical models. Since the simulated spectra agree within percent level with the semi-analytical realization of CAMB, this means that our map-making procedure traces with good accuracy the evolving matter distribution.



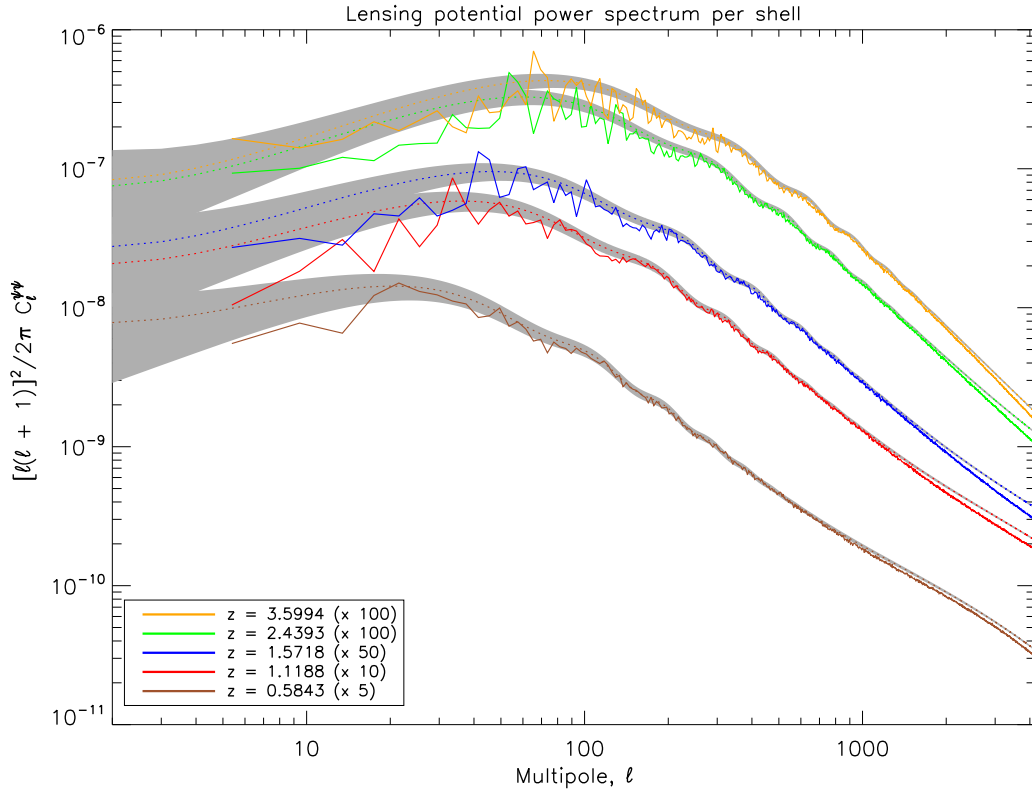


**Figure 5:** Comparison between the angular power spectrum of the lensing potential computed with our algorithm (solid lines) and the analytical results obtained using the Limber equation (dotted lines) at different redshift. The spectra have been multiplied by a constant factor for displaying purposes. The grey area displays the cosmic variance  $1\sigma$  uncertainty for the theoretical spectra.

## 5 Results

### 5.1 Numerical effects of the pixel-based methods

Pixel-based methods for CMB lensing, though in general very efficient, are subjected to several numerical problems. The first one is related to the bandwidths of the lensed CMB fields generated as a result of the calculation. Because the lensing effect happens before the intervention of any instrumental response, the synthesis and analysis of relevant sky signals in the pixel-based lensing methods (CMB source plane and lensing potential map) require using a resolution sufficient to support the signal up to the intrinsic bandwidth  $\ell_{max}$  set by the user specific application and its required accuracy. However, since mathematically the lensing effects act as a convolution in the harmonic domain, the bandwidth of the resulting lensed field is broader than the one of the unlensed CMB and of the lensing potential. Therefore, given the bandwidth used to synthesize the CMB source plane ( $\ell_{max}^{CMB}$ ), i.e before undergoing any deflection, and the one used to solve the Poisson equation and to create the deflection field for a given shell ( $\ell_{max}^{\psi}$ ), the resulting lensed CMB will have an approximate band-limit

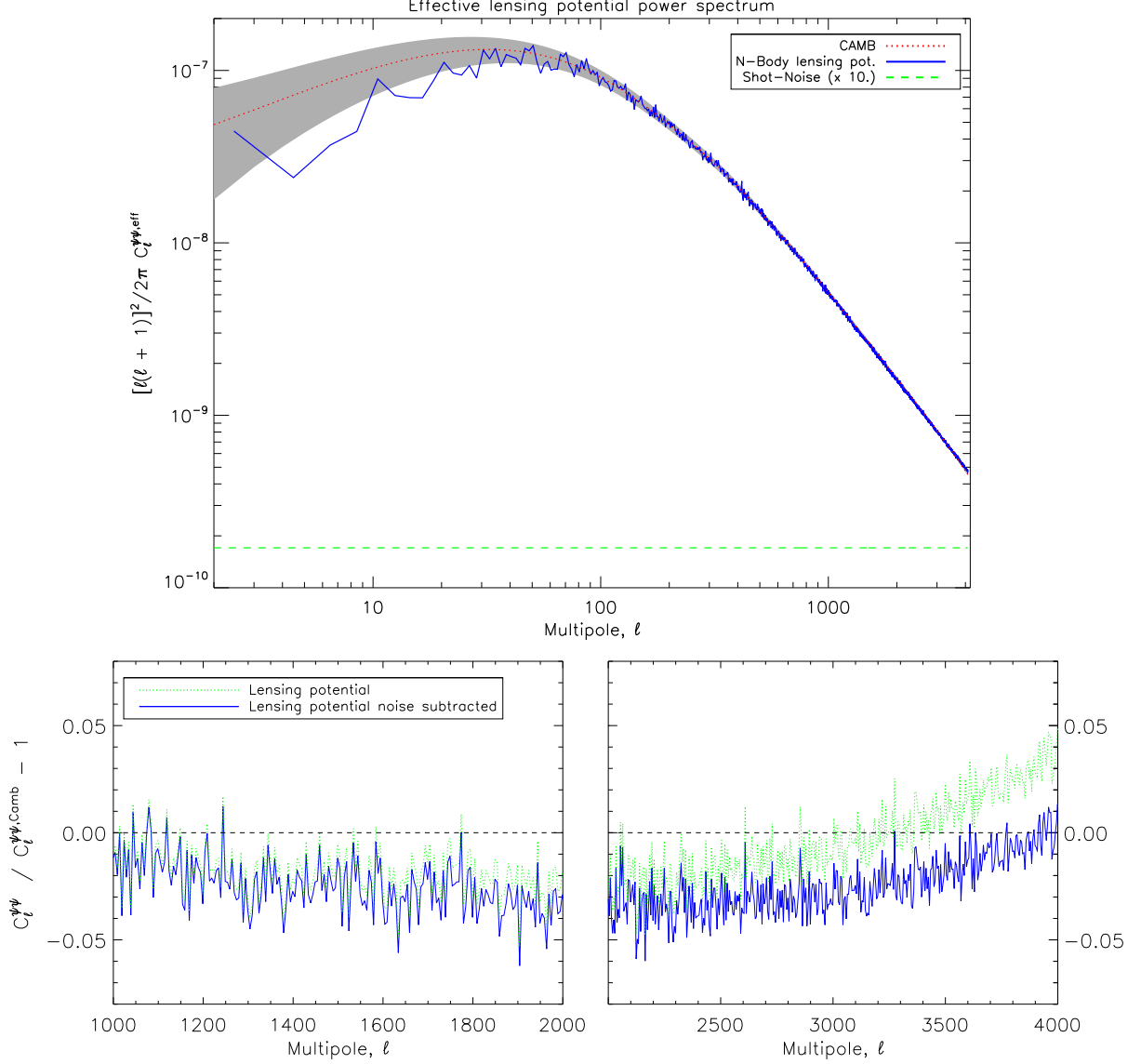


**Figure 6:** Top panel: Integrated lensing potential  $\psi^{eff}$  obtained in the Born approximation from the simulation (green) and the CAMB result based on semi-analytical approximation of the non-linear evolution (red). The fractional difference between the two is displayed for some intermediate and high multipoles scales in the bottom panels. The results obtained after the shot-noise subtraction are displayed in blue solid lines. Note that the shot-noise spectrum in the top panel is multiplied by an arbitrary factor of 10 to be seen clearly in the Figure.

of  $\ell_{max}^{CMB} + \ell_{max}^{\psi}$ <sup>8</sup>. Consequently, the lensed map should have its resolution appropriately chosen to eliminate potential power aliasing effects on these angular scales [54]. We note moreover that these aliasing effects are even more important in the case of the ML approach because the bandwidth extension induced by lensing happens each time the lensed CMB is

<sup>8</sup>We note that in general this bandlimit is only approximate and the resulting function is strictly not band-limited unlike the input source plane.

propagated through a single shell.

The second challenge arises from the fact that the displaced direction at each iteration  $\hat{\mathbf{n}}'^{(k)}$  does not correspond in general to the pixel centers of any iso-latitudinal grid on the sphere. The values of the CMB signal at those locations thus cannot be computed with the aid of fast SHT algorithm and a more elaborated approach is needed. In the context of pixel-based simulation methods, interpolation is the most popular workaround of the need to directly calculate values of the unlensed fields for every displaced directions. The exact solution, which consist in a direct resummation of the spherical harmonics at the displaced position, is in fact unfeasible even for moderate resolutions [53, 54]. Any interpolation in this context, however, is not without its dangers because interpolations tend to smooth the underlying signals and - as a consequence - to hide aliasing effects in the lensed maps. For this reason we chose the bandwidth of our signal ( $\ell_{max}^{CMB} = \ell_{max}^{\psi} = 4096$ ) and the resolution of our grid (NSIDE=4096) following the recipe provided in [54] to minimize all of these effects simultaneously. This choice however limits the multipole range where the lensing signal can be reproduced with high reliability especially in the case of B-modes of polarization to  $\ell \lesssim 2500$  (see Sec 5.3).

## 5.2 Shot-noise contribution

In this section we estimate the impact of the intrinsic discretisation of the N-Body simulation on the final lensed CMB power spectra. Since we expect changes in the power spectrum on the order of few percent, it is mandatory to be able to control numerical artifacts with the same level of precision. For this study we use the analytical modelling of weak lensing in the harmonic domain discussed in [48]. This treats lensing as an effective convolution in Fourier space between the unlensed CMB and the lensing potential and it is based on a second order Taylor expansion around the unperturbed photons direction. The formulae are accurate to better than the percent level on the angular scales considered in this work, especially in the case of B-modes, and allow to quantify more easily the impact of the choice of the band-limit on the recovered result. In the specific case of B-modes, the convolution reads:

$$\tilde{C}_{\ell_B}^{BB} = O(\tilde{\ell}_B, C_{\ell}^{\psi\psi}) \cdot C_{\ell_B}^{BB} + \frac{1}{2} \sum_{\ell_E, \ell_{\psi}} \frac{|2F_{\tilde{\ell}_B \ell_E \ell_{\psi}}|^2}{(2\tilde{\ell}_B + 1)} C_{\ell_{\psi}}^{\psi\psi} [C_{\ell_E}^{EE}(1 - (-1)^L) + C_{\ell_E}^{BB}(1 + (-1)^L)], \quad (5.1)$$

where we denote with tilde a lensed quantity and  $L = \tilde{\ell}_B + \ell_E + \ell_{\psi}$ . We refer the reader to [54] for a detailed discussion of the properties of the convolution kernels  $F_{\tilde{\ell}_B \ell_E \ell_{\psi}}$  and to the  $O(\tilde{\ell}_B, C_{\ell}^{\psi\psi})$  factor. Similar expression can also be derived for the TT, TE and EE power spectra [48]. Since this formalism does not make any assumption on the explicit form nor the origin of  $C_{\ell}^{\psi\psi}$ , we can plug in Eq. (5.1) the shot-noise power spectrum instead of the lensing potential extracted from the N-body simulation, to estimate the fraction of the recovered signal generated by the limited resolution of our simulated data. For this purpose we truncated the sum of Eq. (5.1) to the same band-limit value used in the lensing simulation, i.e.  $\ell_{max}^E = \ell_{max}^{\psi} = 4096$ .

We first evaluate the shot-noise contribution to the  $\psi^{eff}$  lensing potential starting from Eq. (4.3) and assuming the average number density to be the one of the  $\psi^{eff}$  field,  $\bar{n}_k^{eff}$ . This is then used as an input for the analytical formulae of Eq. (5.1), assuming the primordial B-modes  $C_{\ell}^{BB}$  to be zero as it is the case for the unlensed CMB realizations used in the following. To validate the analytical shot-noise predictions we also produce 100 Monte Carlo realizations of shot-noise for the effective lensing potential. We use those maps to extract a

deflection field which is then given as input to `LensPix` to lens a random realization of the CMB signal. The final average of all the power spectra of these set of lensed CMB maps contains thus only the lensing effect due to the shot-noise acting on primordial anisotropies. To evaluate the shot-noise contribution to the ML method we compute Eq. (4.3) for each  $k$ -shell and then apply the analytical convolution iteratively assuming as input CMB spectrum for the  $k$ -th shell the lensed one emerging from lensing of the previous  $(k - 1)$ -th iteration. As discussed in the following section, if we assume a power cut-off for the incoming CMB and the lensing potential to be  $\ell_{max}^{CMB}$  and  $\ell_{max}^{\psi}$  respectively, the lensed CMB after each deflection shows power up to a multipole  $\tilde{\ell} \approx \ell_{max}^{CMB} + \ell_{max}^{\psi}$ , due to the properties of the lensing convolution kernels in the harmonic domain [54]. The evaluation of the lensing kernels requires in fact a computationally-heavy summation of Wigner-3j symbols up to high multipoles. We therefore have assumed that for the iteration  $k > 0$  the incoming CMB has power at most up to  $\ell = 8192$ . This additional cutoff is high enough not to affect significantly the results on the scale considered in this work. The analytical formulae were validated also in this case with Monte Carlo simulation where for each shell the noise realizations were generated starting from the shot-noise power spectrum of the single shell.

In Figure 7 we show the results obtained from both these methods, for the B-mode power spectrum, which is the most sensitive to the details of the lensing potential being entirely lens-induced in our case (no primordial tensor modes). The TT and EE spectra are conversely quite insensitive to the the shot-noise which impacts the results at the sub 0.1% level (see Figure 8). Both the analytical and Monte Carlo estimates of the shot-noise contribution in the Born approximation agree extremely well at all angular scales. The shot-noise contribution in the ML approach is comparable to the effective case at  $\ell \lesssim 2000$  though the difference is less than 0.5%.

### 5.3 Angular power spectrum

Similarly to the case of the lensing potential extraction, we now take into consideration two different approaches also for the evaluation of the angular power spectrum of the lensed CMB. The first set of primary CMB maps are lensed in the Born approximation, while the second set by mean of the ML approach. In Figure 8 we show the comparison between the expected CMB lensed temperature and the E-modes of polarization power spectra, ( $C_{\ell}^{TT}$  and  $C_{\ell}^{EE}$ ), estimated using semi-analytical halo mass function implemented in `CAMB` [57, 58], and the spectra extracted from our lensed CMB maps. For both these cases the simulated power spectra follows precisely the `CAMB` signal. In particular, the shot-noise-induced contribution (evaluated following the recipe of the Section 5.2) for these two observables is negligible given that the effect of lensing per-se is already minor. Thus, changes introduced at percent variation in the lensing potential are further mitigated and hidden in the numerical noise. After having subtracted the shot-noise induced lensing contribution, the fractional difference between `CAMB` and the N-Body lensed spectra shows no significant bias up to  $\ell \approx 3000$  where we start seeing effects due to the choice of  $\ell_{max}^{CMB}$ . The latter is not high enough to properly resolve power on those scales with high-accuracy. The difference between the results obtained with the Born and ML method is negligible and important only towards scales  $\ell \approx \ell_{max}$  (see Figure 9). The abrupt decrease in power observed on those scales for the ML approach with respect to the Born approximation is due to the effect of polynomial interpolation. As the latter tends to smooth the underlying signal, the consecutive application effectively removes more power on small angular scale with respect to the Born approach, for which the interpolation is performed only once.

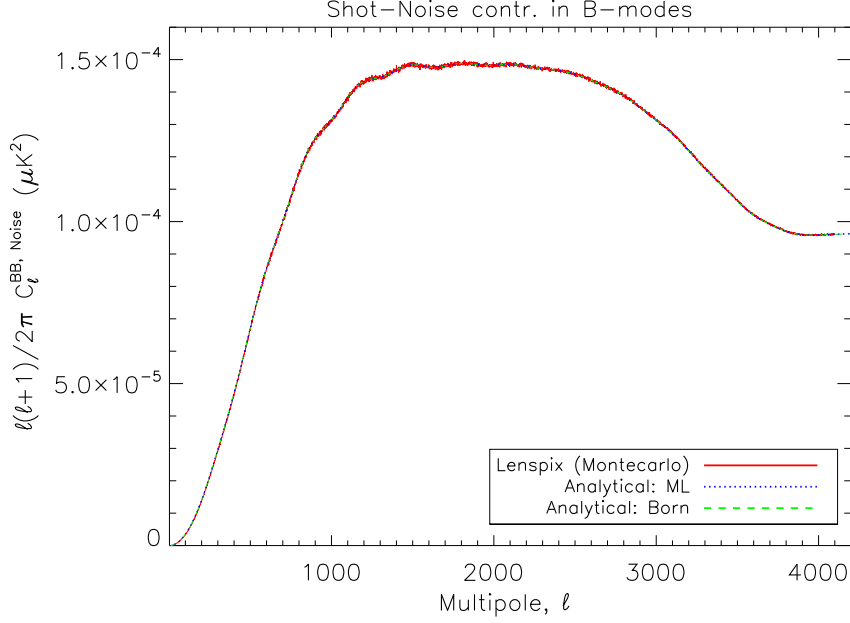


**Figure 7:** Angular power spectrum for the lensed B-modes induced by the simulation shot-noise. The red, solid line is computed using 100 realizations of the algorithm in the Born approximation scenario. The green-dotted and the blue-dashed lines are evaluated with the analytical formula for - respectively - the Born and the multiple plane scenario.

The situation however is different for the B-modes of polarization, as shown in Figure 10. This signal is entirely caused by lensing as we have set the primordial tensor modes to zero. Its behaviour is therefore a clear imprint of how the LSS process the primary CMB field and thus we expect this observable to reflect more directly the features observed in the lensing potential. As expected from the analysis of the lensing potential in Section 4.2, the BB spectrum shows a lack of power at percent level with respect to CAMB spectra, in agreement with the matter power spectrum of the N-Body simulation, though this effect is partially compensated by the increase in power at small scales in the lensing potential. This feature is not observable in the lensed T or E field, where power coming from primordial anisotropies is dominant over the lensing-induced one. Moreover, while negligible in the TT and EE cases, we found the shot-noise contribution to be important at the percent level for the BB power spectrum at small scales. This is expected given that B-modes are very sensitive to non-linear power, which is affected by shot-noise for  $\ell \gg 2000$  (see bottom panel of Figure 6). The lack of power due to the choice of  $\ell_{max}^{CMB}$  starts to be important on angular scales larger than the ones affected in T and E-modes power spectra. This can be explained considering that at those scales a non-negligible fraction of the contribution to the BB power spectrum starts to come from progressively higher multipoles of both E and  $\psi$ . At  $\ell_B \sim 4000$ , for instance, a 25% contribution to the power in the B-modes comes from scales in the E and  $\psi$  fields at  $\ell > \ell_{max} = 4096$  [54]. Since our algorithm is band-limited to this  $\ell_{max}$ , cutting power for those high  $\ell$ , produce a loss of about 25% in the BB power spectrum at that particular multipole (as shown in Figure 10).

As argued in Section 5.1, one of the major numerical problem affecting the simulation of CMB B-modes is the power aliasing due to bandwidth extension induced by lensing. In

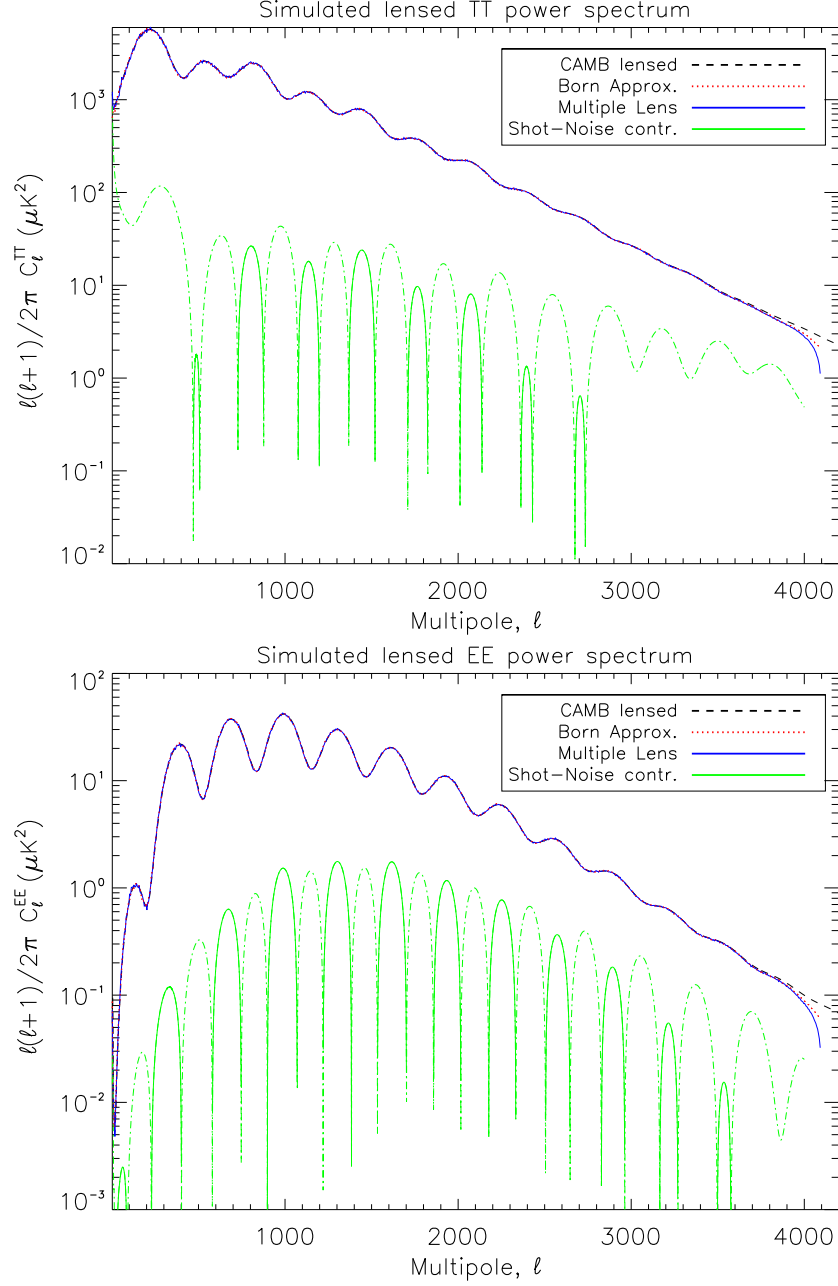


**Figure 8:** Angular power spectrum of the (lensed) total intensity T (top panel) and the E-mode polarization of the CMB (bottom panel). Black dashed lines are CAMB realization of a lensed spectra. Red dotted line uses the lensing field as in the Born approximation, while for the blue solid line the CMB is lensed through multiple planes. Green lines in both panels show the shot-noise contribution to the lensed TT and EE spectra; green, dot-dashed lines represent the absolute value of this contribution.

Figure 11 we show the impact of this effect as a function of the map resolution on the B-modes power spectrum recovery. For this tests we extracted the lensing potential maps for both Born and ML approach using two different HEALPix grid at  $\text{NSIDE} = 2048, 4096$  and

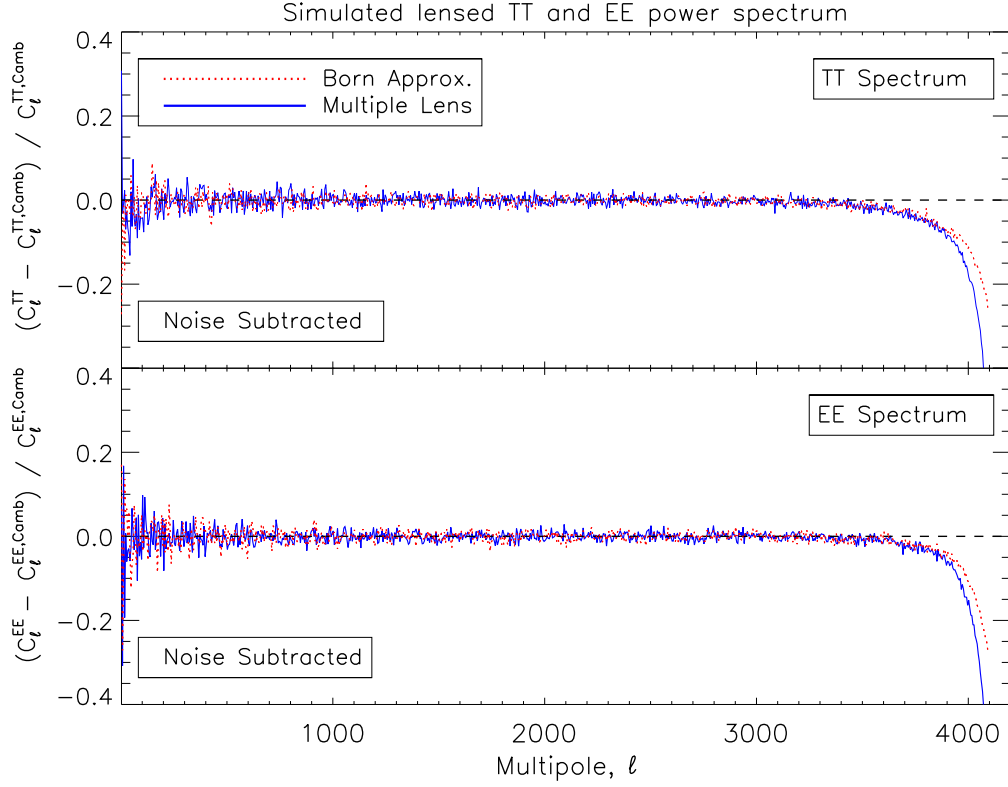


**Figure 9:** Fractional difference for the angular power spectrum of the temperature (top panel) and E-mode polarization (bottom panel) with respect to `CAMB`. Red dotted lines are obtained in the Born approximation, while blue solid in the multiple lens plane approach. The shot-noise has been subtracted in both cases.

refer to these two setup as the low and high resolution case respectively. We then synthesized on the same grid the CMB source plane assuming the same bandlimit  $\ell_{max}^{CMB} = 4096$ , as done for the results discussed above, and propagate it through the lensing plane(s). As shown in Figure 11, the Born approximation method is quite insensitive to the choice of `NSIDE` because the polynomial interpolation is effective in removing most of the aliasing. However, for the ML scenario the situation is worse as the aliasing generated by multiple deflection can add up, becoming progressively more important. This can then lead to a misinterpretation of the result obtained using the ML, which seems to be significantly different from the once obtained in the Born approximation. The fact that this difference vanishes in the high-resolution case is a demonstration of the high level of control of numerical effects which needs to be achieved for this kind of algorithms. Even though these effects were limited in the setup considered here, we expect those to become more important when targeting accurate lensing simulations on scales  $\ell \gg 2000$ .

Finally, we compare the differences in the angular power spectra between the Born approximation and the multiple planes approach. First we define the quantity  $O_\ell^X$  as the difference between the angular power spectra extracted with the multiple lens approach and



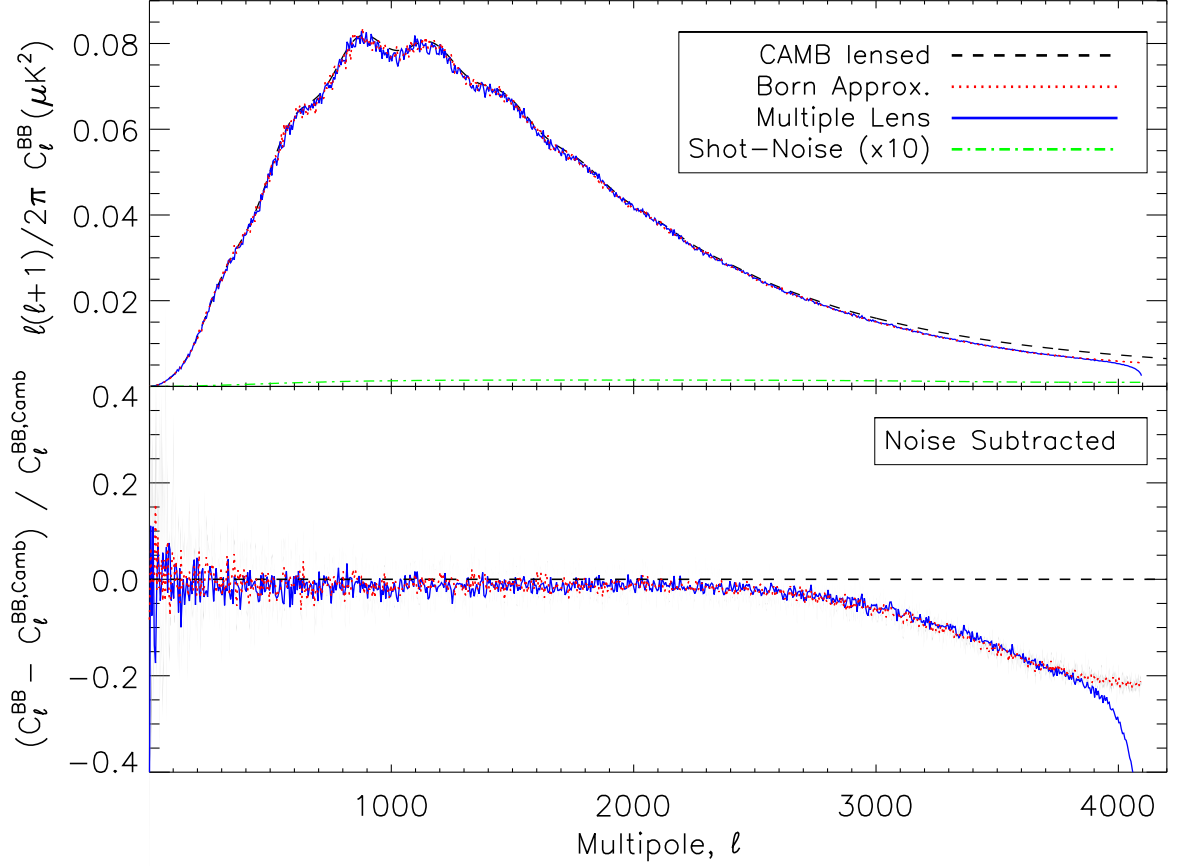


**Figure 10:** Angular power spectrum for the B-mode polarization of CMB. Black dashed lines are CAMB realization of a lensed spectra. Red dotted lines are obtained in the Born approximation, while blue solid lines in the multiple lens planes approach. The green dot-dashed line is a lensed spectrum produced from a shot-noise-only lensing map. In the bottom panel, it is shown the fractional difference with the reference CAMB spectrum. In this panel, the noise power spectrum has been subtracted from the original signal.

the one computed in the Born approximation,

$$O_\ell^X = C_\ell^{X,ML} - C_\ell^{X,Born}, \quad (5.2)$$

where  $X = TT, EE, BB$ . Its uncertainty is given by the cosmic variance affecting both spectra, or

$$\sigma_{O_\ell^X} = \sqrt{\frac{2}{2\ell+1} (|C_\ell^{X,ML}|^2 + |C_\ell^{X,Born}|^2)}. \quad (5.3)$$

Starting from these quantities we can define a reduced chi-square  $\tilde{\chi}^2$  statistics

$$\tilde{\chi}^2 = \frac{1}{\ell_{max} - 1} \sum_{\ell=2}^{\ell_{max}} \frac{O_\ell^2}{\sigma_{O_\ell}^2}, \quad (5.4)$$

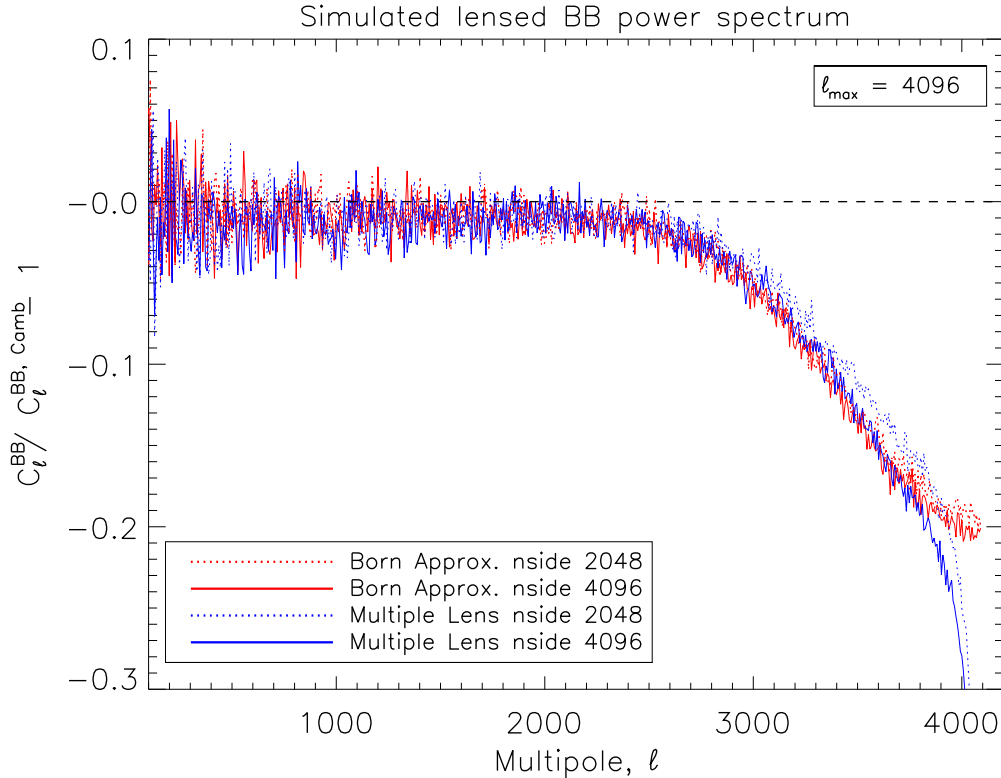


**Figure 11:** Fractional difference of angular power spectrum of the BB power spectrum with respect to the reference **CAMB** spectrum. Dotted lines refers to the map at low resolution ( $N_{\text{SIDE}}=2048$ ), while solid lines to the map with  $N_{\text{SIDE}}=4096$ . Red lines plot the effective, Born approximation case, blue lines are connected to the multiple plane approach. Note that for this comparison, the noise power spectrum has not been subtracted from the original signal.

to assess whether the two methods are inconsistent. Since we expect  $O_\ell^X / \sigma_{O_\ell}^2$  to be a Gaussian random variable, we can also perform a Kolmogorov-Smirnov (KS) to test whether this hypothesis is verified or systematic differences exists between the two methods. In defining both these tests and the sample variance of Eq. (5.4), we assumed that the covariance of the lensed power spectra is Gaussian. This assumption neglects the fact that lensing introduces non-Gaussian correlations between different modes [59, 60], but this effect is mainly important for B-modes, for which the gaussianity assumption underestimates the sample variance.

In Table 1 we report the results of both those tests expressed as the significance level probability. In both cases we find that the power spectra obtained in the Born approximation and with the ML method are statistically consistent. A further possible test to compare the two methods would be to reconstruct the effective integrated matter density from the simulated lensed CMB maps as done in [36], but we leave this option to future work.

## 6 Discussion and Conclusions

We have developed and tested a new algorithm to study the gravitational lensing of the CMB on the full sky. Starting from snapshots of an N-Body simulation, we reconstructed

$C_\ell^X$	Significance $P_{KS}$	Significance $P_{\tilde{\chi}^2}$
TT	0.47	0.70
EE	0.19	0.51
BB	0.21	0.19

**Table 1:** Results of statistical tests on difference between lensed CMB angular power spectra in the Born approximation and multiple lens planes approach. The significance level probability for the null hypothesis using a Kolmogorov-Smirnov test ( $P_{KS}$ ) and a reduced chi-square  $\tilde{\chi}^2$  statistics ( $P_{\tilde{\chi}^2}$ ) show no difference between the power spectra computed with the two methods on a statistical level.

the whole lightcone around the observer between  $z \in [0, 10]$  overcoming the finite size of N-Body box through the box stacking technique developed in [50]. We sliced the lightcone into 25 different spherical maps onto which the matter distribution was projected. The spherical shells were then used as source planes to lens the incoming CMB photons either adopting an effective method based on the Born approximation or using a multiple-lens ray-tracing approach. This is, to our knowledge, the first attempt to apply this kind of algorithm to the CMB polarization. For this reason, we performed a detailed analysis of the numerical effects involved in the ML method coming both from the N-Body simulation and from the ray-tracing procedure itself. The Born approximation, which has been widely tested in the literature, was used as benchmark to highlight the multiple-lens range of validity and to assess its virtues in reproducing non-linearities from the N-Body simulation at small scales. In particular, the projection of the N-Body matter distribution onto concentric spherical maps allows to compress all the interesting information from the N-Body simulation into a more manageable lightcone, mimicking a realistic distribution of large scale structure as observed by present and future large galaxy surveys.

We validated the lensing planes reconstruction both on the map level and on the statistical level using the 2-point correlation function in the harmonic domain evaluated for all the spherical maps constructed across the past lightcone. We found the latter to be reproduced fairly well by semi-analytical approximations to the non-linear evolution implemented in widely used Boltzmann codes, though deviations at the percent level were clearly observed. We also analysed the final, lensed CMB anisotropies in both temperature and polarization for the effective as well as the multiple plane approach, paying a particular attention to the B-modes of polarization. These are in fact the most sensitive quantities both to the overall lensing process and to the numerical effects. In the latter case, we discussed in detail how to minimize their impact. We found however that these numerical effects are usually negligible for the temperature and E-modes polarization field and important only for B-modes. The B-modes signal was found to be lower than the one computed using the semi-analytical, following the general trend observed in the extracted lensing potential power spectrum.

Finally, we have extended the control of the validity of the Born approximation to the limiting resolution of the present setup of our simulations. Our results indicate that, when checking the angular power spectra of lensing observables, including CMB lensed fields, the latter approximation describes well the ray-tracing performed by the ML approach. However we expect the latter to perform better for studies aiming at investigating the statistics of the signal at smaller angular scales, or in presence of distortion from isolated, sharp structures. The spherical map matter projection, in both the Born approximation and ML implemen-

tations, can be particularly useful in cross-correlation studies between the CMB with other tracers of mass and foreground sources, for characterizing the simulation of mock catalogues of observables built from N-Body simulations. The tomography of LSS, which is an intrinsic feature of the two lensing approaches analysed in this work, can be exploited to investigate different cosmological scenarios, looking at the effects of different DE models on small scales as well on the whole evolution of the matter in Universe. These feature will be of great importance for upcoming projects such as the Euclid satellite that can fully exploit the capabilities of cross-correlation as cosmological probe.

## Acknowledgments

We acknowledge the use of the publicly available Code for Anisotropies in the Microwave Background (CAMB), LensPix and the Hierarchical Equalised Latitude Pixel spherical pixelization scheme (HEALPix). The L-CoDECs simulations were carried out on the Power6 cluster at the RZG computing centre in Garching and on the SP6 machine at the “Centro Interuniversitario del Nord-Est per il Calcolo Elettronico” (CINECA, Bologna). The ray-tracing computations have been performed on the IBM Fermi cluster at CINECA, with CPU time assigned under several CINECA class-C calls, and at the National Energy Research Scientific Computing Center (NERSC), which is supported by the Office of Science of the U.S. Department of Energy under Contract No. DE-AC02-05CH11231. Part of this work was supported by the InDark INFN Grant. CC acknowledges financial support to the “INAF Fellowships Programme 2010” and to the European Research Council through the Darklight Advanced Research Grant (# 291521). MC acknowledges the financial support through the INAF funds for the Euclid mission. MB is supported by the Marie Curie Intra European Fellowship “SIDUN” within the 7th Framework Programme of the European Commission.

## A Measuring angular power spectrum

The lensing potential is extracted from N-body simulation through a binned map-making procedure of particles contained in a sky pixel. For this reason when we want to extract its underlying power spectrum we have to correct for the pixel window function of the HEALPix grid. Assuming an azimuthally symmetric patch, as it is the case for the full sky, the pixel window function is azimuthally symmetric and can be used to correct the pseudo power spectrum extracted from the full sky map using a simple spherical harmonic analysis operation. A continuous field sampled on the HEALPix sphere is a smoothed version of the true underlying field due to the finite pixel size, i.e. the value of the field in pixel  $i$  is given by

$$\Phi^{pix(i)} = \int d^2\hat{\mathbf{n}} w^{(i)}(\hat{\mathbf{n}}) \Phi(\hat{\mathbf{n}}), \quad (\text{A.1})$$

where  $w^{(i)}$  is the window function of the  $i$ -th pixel as is given by

$$w^{(i)}(\hat{\mathbf{n}}) = \begin{cases} \Omega_{pix}^{-1}, & \text{inside pixel } i \\ 0 & \text{elsewhere.} \end{cases} \quad (\text{A.2})$$

Expanding the true field  $\Phi$  in terms of spherical harmonics as

$$\Phi(\hat{\mathbf{n}}) = \sum_{\ell m} \Phi_{\ell m} Y_{\ell m}(\hat{\mathbf{n}}), \quad (\text{A.3})$$

we have

$$\Phi^{pix(i)} = \sum_{\ell m} w_{\ell m}^{(i)} \Phi_{\ell m}; \quad (\text{A.4})$$

where

$$w_{\ell m}^{(i)} = \int d^2 \hat{\mathbf{n}} w^{(i)}(\hat{\mathbf{n}}) Y_{\ell m}(\hat{\mathbf{n}}) \quad (\text{A.5})$$

is the spherical harmonic transform of the pixel window function. The computation of these coefficients for each and every pixel is required for a complete analysis in the `HEALPix` scheme; however this calculation becomes computationally unfeasible, even for a moderate `NSIDE`. Therefore, it is advantageous to ignore the azimuthal variation and rewrite Equation (A.5) as

$$w_{\ell m}^{(i)} = w_{\ell}^{(i)} Y_{\ell m}(\hat{\mathbf{n}}_i), \quad (\text{A.6})$$

defining an azimuthally averaged window function as

$$w_{\ell}^{(i)} = \frac{4\pi}{(2\ell+1)} \left[ \sum_{m=-\ell}^{\ell} |w_{\ell m}|^2 \right]^{1/2}. \quad (\text{A.7})$$

It follows immediately from Equations (A.4) and (A.6) that the estimate of the power spectrum of the pixelated field is given by

$$C_{\ell}^{\Phi, pix} = w_{\ell}^2 \langle \Phi_{\ell m} \Phi_{\ell m}^* \rangle, \quad (\text{A.8})$$

where the pixel averaged window function is defined as

$$w_{\ell} = \left( \frac{1}{N_{pix}} \sum_{i=0}^{N_{pix}-1} \left( w_{\ell}^{(i)} \right)^2 \right)^{1/2}. \quad (\text{A.9})$$

This function is available for  $\ell < 4 \times \text{NSIDE}$  in the `HEALPix` distribution. As we divide the computed power spectrum by the square of the above function, it is possible to correct the effect of the pixel window; in our case we act directly on the spherical harmonics coefficient  $\Phi_{\ell m}$  recovered from our spherical maps, using the actual  $w_{\ell}$ .

## References

- [1] Planck Collaboration, P. A. R. Ade, N. Aghanim, C. Armitage-Caplan, M. Arnaud, M. Ashdown, F. Atrio-Barandela, J. Aumont, C. Baccigalupi, A. J. Banday, and et al., *Planck 2013 results. XVI. Cosmological parameters*, *ArXiv e-prints* (Mar., 2013) [[arXiv:1303.5076](https://arxiv.org/abs/1303.5076)].
- [2] B. Reichborn-Kjennerud, A. M. Aboobaker, P. Ade, F. Aubin, C. Baccigalupi, C. Bao, J. Borrill, C. Cantalupo, D. Chapman, J. Didier, M. Dobbs, J. Grain, W. Grainger, S. Hanany, S. Hillbrand, J. Hubmayr, A. Jaffe, B. Johnson, T. Jones, T. Kisner, J. Klein, A. Korotkov, S. Leach, A. Lee, L. Levinson, M. Limon, K. MacDermid, T. Matsumura, X. Meng, A. Miller, M. Milligan, E. Pascale, D. Polsgrove, N. Ponthieu, K. Raach, I. Sagiv, G. Smecher, F. Stivoli, R. Stompor, H. Tran, M. Tristram, G. S. Tucker, Y. Vinokurov, A. Yadav, M. Zaldarriaga, and K. Zilic, *EBEX: a balloon-borne CMB polarization experiment*, in *Society of Photo-Optical Instrumentation Engineers (SPIE) Conference Series*, vol. 7741 of *Society of Photo-Optical Instrumentation Engineers (SPIE) Conference Series*, July, 2010. [arXiv:1007.3672](https://arxiv.org/abs/1007.3672).

- [3] Z. D. Kermish, P. Ade, A. Anthony, K. Arnold, D. Barron, D. Boettger, J. Borrill, S. Chapman, Y. Chinone, M. A. Dobbs, J. Errard, G. Fabbian, D. Flanigan, G. Fuller, A. Ghribi, W. Grainger, N. Halverson, M. Hasegawa, K. Hattori, M. Hazumi, W. L. Holzapfel, J. Howard, P. Hyland, A. Jaffe, B. Keating, T. Kisner, A. T. Lee, M. Le Jeune, E. Linder, M. Lungu, F. Matsuda, T. Matsumura, X. Meng, N. J. Miller, H. Morii, S. Moyerman, M. J. Myers, H. Nishino, H. Paar, E. Quealy, C. L. Reichardt, P. L. Richards, C. Ross, A. Shimizu, M. Shimon, C. Shimmmin, M. Sholl, P. Siritanasak, H. Spieler, N. Stebor, B. Steinbach, R. Stompor, A. Suzuki, T. Tomaru, C. Tucker, and O. Zahn, *The POLARBEAR experiment*, in *Society of Photo-Optical Instrumentation Engineers (SPIE) Conference Series*, vol. 8452 of *Society of Photo-Optical Instrumentation Engineers (SPIE) Conference Series*, Sept., 2012. [arXiv:1210.7768](#).
- [4] J. E. Austermann, K. A. Aird, J. A. Beall, D. Becker, A. Bender, B. A. Benson, L. E. Bleem, J. Britton, J. E. Carlstrom, C. L. Chang, H. C. Chiang, H.-M. Cho, T. M. Crawford, A. T. Crites, A. Datesman, T. de Haan, M. A. Dobbs, E. M. George, N. W. Halverson, N. Harrington, J. W. Henning, G. C. Hilton, G. P. Holder, W. L. Holzapfel, S. Hoover, N. Huang, J. Hubmayr, K. D. Irwin, R. Keisler, J. Kennedy, L. Knox, A. T. Lee, E. Leitch, D. Li, M. Lueker, D. P. Marrone, J. J. McMahon, J. Mehl, S. S. Meyer, T. E. Montroy, T. Natoli, J. P. Nibarger, M. D. Niemack, V. Novosad, S. Padin, C. Pryke, C. L. Reichardt, J. E. Ruhl, B. R. Saliwanchik, J. T. Sayre, K. K. Schaffer, E. Shirokoff, A. A. Stark, K. Story, K. Vanderlinde, J. D. Vieira, G. Wang, R. Williamson, V. Yefremenko, K. W. Yoon, and O. Zahn, *SPTpol: an instrument for CMB polarization measurements with the South Pole Telescope*, in *Society of Photo-Optical Instrumentation Engineers (SPIE) Conference Series*, vol. 8452 of *Society of Photo-Optical Instrumentation Engineers (SPIE) Conference Series*, Sept., 2012. [arXiv:1210.4970](#).
- [5] M. D. Niemack, P. A. R. Ade, J. Aguirre, F. Barrientos, J. A. Beall, J. R. Bond, J. Britton, H. M. Cho, S. Das, M. J. Devlin, S. Dicker, J. Dunkley, R. Dünner, J. W. Fowler, A. Hajian, M. Halpern, M. Hasselfield, G. C. Hilton, M. Hilton, J. Hubmayr, J. P. Hughes, L. Infante, K. D. Irwin, N. Jarosik, J. Klein, A. Kosowsky, T. A. Marriage, J. McMahon, F. Menanteau, K. Moodley, J. P. Nibarger, M. R. Nolte, L. A. Page, B. Partridge, E. D. Reese, J. Sievers, D. N. Spergel, S. T. Staggs, R. Thornton, C. Tucker, E. Wollack, and K. W. Yoon, *ACTPol: a polarization-sensitive receiver for the Atacama Cosmology Telescope*, in *Society of Photo-Optical Instrumentation Engineers (SPIE) Conference Series*, vol. 7741 of *Society of Photo-Optical Instrumentation Engineers (SPIE) Conference Series*, July, 2010. [arXiv:1006.5049](#).
- [6] A. A. Fraisse, P. A. R. Ade, M. Amiri, S. J. Benton, J. J. Bock, J. R. Bond, J. A. Bonetti, S. Bryan, B. Burger, H. C. Chiang, C. N. Clark, C. R. Contaldi, B. P. Crill, G. Davis, O. Doré, M. Farhang, J. P. Filippini, L. M. Fissel, N. N. Gandilo, S. Golwala, J. E. Gudmundsson, M. Hasselfield, G. Hilton, W. Holmes, V. V. Hristov, K. Irwin, W. C. Jones, C. L. Kuo, C. J. MacTavish, P. V. Mason, T. E. Montroy, T. A. Morford, C. B. Netterfield, D. T. O’Dea, A. S. Rahlin, C. Reintsema, J. E. Ruhl, M. C. Runyan, M. A. Schenker, J. A. Shariff, J. D. Soler, A. Trangsrud, C. Tucker, R. S. Tucker, A. D. Turner, and D. Wiebe, *SPIDER: probing the early Universe with a suborbital polarimeter*, *JCAP* **4** (Apr., 2013) 47, [[arXiv:1106.3087](#)].
- [7] C. D. Sheehy, P. A. R. Ade, R. W. Aikin, M. Amiri, S. Benton, C. Bischoff, J. J. Bock, J. A. Bonetti, J. A. Brevik, B. Burger, C. D. Dowell, L. Duband, J. P. Filippini, S. R. Golwala, M. Halpern, M. Hasselfield, G. Hilton, V. V. Hristov, K. Irwin, J. P. Kaufman, B. G. Keating, J. M. Kovac, C. L. Kuo, A. E. Lange, E. M. Leitch, M. Lueker, C. B. Netterfield, H. T. Nguyen, R. W. Ogburn, IV, A. Orlando, C. L. Pryke, C. Reintsema, S. Richter, J. E. Ruhl, M. C. Runyan, Z. Staniszewski, S. Stokes, R. Sudiwala, G. Teply, K. L. Thompson, J. E. Tolán, A. D. Turner, P. Wilson, and C. L. Wong, *The Keck Array: a pulse tube cooled CMB polarimeter*, *ArXiv e-prints* (Apr., 2011) [[arXiv:1104.5516](#)].
- [8] M. Zaldarriaga and U. Seljak, *All-sky analysis of polarization in the microwave background*, *Phys. Rev. D* **55** (Feb., 1997) 1830–1840, [[astro-ph/9609170](#)].
- [9] M. Kamionkowski, A. Kosowsky, and A. Stebbins, *Statistics of cosmic microwave background*



polarization, *Phys. Rev. D* **55** (June, 1997) 7368–7388, [[astro-ph/9611125](#)].

- [10] U. Seljak and M. Zaldarriaga, *Signature of Gravity Waves in the Polarization of the Microwave Background*, *Physical Review Letters* **78** (Mar., 1997) 2054–2057, [[astro-ph/9609169](#)].
- [11] BICEP2 Collaboration, P. A. R. Ade, R. W. Aikin, M. Amiri, D. Barkats, S. J. Benton, C. A. Bischoff, J. J. Bock, J. A. Brevik, I. Buder, E. Bullock, G. Davis, C. D. Dowell, L. Duband, J. P. Filippini, S. Fliescher, S. R. Golwala, M. Halpern, M. Hasselfield, S. R. Hildebrandt, G. C. Hilton, V. V. Hristov, K. D. Irwin, K. S. Karkare, J. P. Kaufman, B. G. Keating, S. A. Kernasovskiy, J. M. Kovac, C. L. Kuo, E. M. Leitch, N. Llombart, M. Lueker, C. B. Netterfield, H. T. Nguyen, R. O’Brien, R. W. Ogburn, IV, A. Orlando, C. Pryke, C. D. Reintsema, S. Richter, R. Schwarz, C. D. Sheehy, Z. K. Staniszewski, K. T. Story, R. V. Sudiwala, G. P. Teply, J. E. Tolán, A. D. Turner, A. G. Vieregg, P. Wilson, C. L. Wong, and K. W. Yoon, *BICEP2 II: Experiment and Three-Year Data Set*, *ArXiv e-prints* (Mar., 2014) [[arXiv:1403.4302](#)].
- [12] R. Flauger, J. C. Hill, and D. N. Spergel, *Toward an understanding of foreground emission in the BICEP2 region*, *JCAP* **8** (Aug., 2014) 39, [[arXiv:1405.7351](#)].
- [13] N. Aghanim, S. Majumdar, and J. Silk, *Secondary anisotropies of the CMB*, *Reports on Progress in Physics* **71** (June, 2008) 066902, [[arXiv:0711.0518](#)].
- [14] A. Lewis and A. Challinor, *Weak gravitational lensing of the CMB*, *Physics Reports* **429** (June, 2006) 1–65, [[astro-ph/0601594](#)].
- [15] S. Das, B. D. Sherwin, P. Aguirre, J. W. Appel, J. R. Bond, C. S. Carvalho, M. J. Devlin, J. Dunkley, R. Dünner, T. Essinger-Hileman, J. W. Fowler, A. Hajian, M. Halpern, M. Hasselfield, A. D. Hincks, R. Hlozek, K. M. Huffenberger, J. P. Hughes, K. D. Irwin, J. Klein, A. Kosowsky, R. H. Lupton, T. A. Marriage, D. Marsden, F. Menanteau, K. Moodley, M. D. Niemack, M. R. Nolta, L. A. Page, L. Parker, E. D. Reese, B. L. Schmitt, N. Sehgal, J. Sievers, D. N. Spergel, S. T. Staggs, D. S. Swetz, E. R. Switzer, R. Thornton, K. Visnjic, and E. Wollack, *Detection of the Power Spectrum of Cosmic Microwave Background Lensing by the Atacama Cosmology Telescope*, *Physical Review Letters* **107** (July, 2011) 021301, [[arXiv:1103.2124](#)].
- [16] R. Keisler, C. L. Reichardt, K. A. Aird, B. A. Benson, L. E. Bleem, J. E. Carlstrom, C. L. Chang, H. M. Cho, T. M. Crawford, A. T. Crites, T. de Haan, M. A. Dobbs, J. Dudley, E. M. George, N. W. Halverson, G. P. Holder, W. L. Holzapfel, S. Hoover, Z. Hou, J. D. Hrubes, M. Joy, L. Knox, A. T. Lee, E. M. Leitch, M. Lueker, D. Luong-Van, J. J. McMahon, J. Mehl, S. S. Meyer, M. Millea, J. J. Mohr, T. E. Montroy, T. Natoli, S. Padin, T. Plagge, C. Pryke, J. E. Ruhl, K. K. Schaffer, L. Shaw, E. Shirokoff, H. G. Spieler, Z. Staniszewski, A. A. Stark, K. Story, A. van Engelen, K. Vanderlinde, J. D. Vieira, R. Williamson, and O. Zahn, *A Measurement of the Damping Tail of the Cosmic Microwave Background Power Spectrum with the South Pole Telescope*, *ApJ* **743** (Dec., 2011) 28, [[arXiv:1105.3182](#)].
- [17] A. van Engelen, R. Keisler, O. Zahn, K. A. Aird, B. A. Benson, L. E. Bleem, J. E. Carlstrom, C. L. Chang, H. M. Cho, T. M. Crawford, A. T. Crites, T. de Haan, M. A. Dobbs, J. Dudley, E. M. George, N. W. Halverson, G. P. Holder, W. L. Holzapfel, S. Hoover, Z. Hou, J. D. Hrubes, M. Joy, L. Knox, A. T. Lee, E. M. Leitch, M. Lueker, D. Luong-Van, J. J. McMahon, J. Mehl, S. S. Meyer, M. Millea, J. J. Mohr, T. E. Montroy, T. Natoli, S. Padin, T. Plagge, C. Pryke, C. L. Reichardt, J. E. Ruhl, J. T. Sayre, K. K. Schaffer, L. Shaw, E. Shirokoff, H. G. Spieler, Z. Staniszewski, A. A. Stark, K. Story, K. Vanderlinde, J. D. Vieira, and R. Williamson, *A Measurement of Gravitational Lensing of the Microwave Background Using South Pole Telescope Data*, *ApJ* **756** (Sept., 2012) 142, [[arXiv:1202.0546](#)].
- [18] POLARBEAR Collaboration, P. A. R. Ade, Y. Akiba, A. E. Anthony, K. Arnold, M. Atlas, D. Barron, D. Boettger, J. Borrill, S. Chapman, Y. Chinone, M. Dobbs, T. Elleflot, J. Errard, G. Fabbian, C. Feng, D. Flanagan, A. Gilbert, W. Grainger, N. W. Halverson, M. Hasegawa,



- K. Hattori, M. Hazumi, W. L. Holzapfel, Y. Hori, J. Howard, P. Hyland, Y. Inoue, G. C. Jaehnig, A. Jaffe, B. Keating, Z. Kermish, R. Keskitalo, T. Kisner, M. Le Jeune, A. T. Lee, E. Linder, E. M. Leitch, M. Lungu, F. Matsuda, T. Matsumura, X. Meng, N. J. Miller, H. Morii, S. Moyerman, M. J. Myers, M. Navaroli, H. Nishino, H. Paar, J. Peloton, E. Quealy, G. Rebeiz, C. L. Reichardt, P. L. Richards, C. Ross, I. Schanning, D. E. Schenck, B. Sherwin, A. Shimizu, C. Shimmin, M. Shimon, P. Siritanasak, G. Smecher, H. Spieler, N. Stebor, B. Steinbach, R. Stompor, A. Suzuki, S. Takakura, T. Tomaru, B. Wilson, A. Yadav, and O. Zahn, *Measurement of the Cosmic Microwave Background Polarization Lensing Power Spectrum with the POLARBEAR experiment*, *ArXiv e-prints* (Dec., 2013) [[arXiv:1312.6646](#)].
- [19] The POLARBEAR Collaboration, P. A. R. Ade, Y. Akiba, A. E. Anthony, K. Arnold, M. Atlas, D. Barron, D. Boettger, J. Borrill, S. Chapman, Y. Chinone, M. Dobbs, T. Elleflot, J. Errard, G. Fabbian, C. Feng, D. Flanagan, A. Gilbert, W. Grainger, N. W. Halverson, M. Hasegawa, K. Hattori, M. Hazumi, W. L. Holzapfel, Y. Hori, J. Howard, P. Hyland, Y. Inoue, G. C. Jaehnig, A. H. Jaffe, B. Keating, Z. Kermish, R. Keskitalo, T. Kisner, M. Le Jeune, A. T. Lee, E. M. Leitch, E. Linder, M. Lungu, F. Matsuda, T. Matsumura, X. Meng, N. J. Miller, H. Morii, S. Moyerman, M. J. Myers, M. Navaroli, H. Nishino, H. Paar, J. Peloton, D. Poletti, E. Quealy, G. Rebeiz, C. L. Reichardt, P. L. Richards, C. Ross, I. Schanning, D. E. Schenck, B. D. Sherwin, A. Shimizu, C. Shimmin, M. Shimon, P. Siritanasak, G. Smecher, H. Spieler, N. Stebor, B. Steinbach, R. Stompor, A. Suzuki, S. Takakura, T. Tomaru, B. Wilson, A. Yadav, and O. Zahn, *A Measurement of the Cosmic Microwave Background B-Mode Polarization Power Spectrum at Sub-Degree Scales with POLARBEAR*, *ArXiv e-prints* (Mar., 2014) [[arXiv:1403.2369](#)].
- [20] D. Hanson, S. Hoover, A. Crites, P. A. R. Ade, K. A. Aird, J. E. Austermann, J. A. Beall, A. N. Bender, B. A. Benson, L. E. Bleem, J. J. Bock, J. E. Carlstrom, C. L. Chang, H. C. Chiang, H.-M. Cho, A. Conley, T. M. Crawford, T. de Haan, M. A. Dobbs, W. Everett, J. Gallicchio, J. Gao, E. M. George, N. W. Halverson, N. Harrington, J. W. Henning, G. C. Hilton, G. P. Holder, W. L. Holzapfel, J. D. Hrubes, N. Huang, J. Hubmayr, K. D. Irwin, R. Keisler, L. Knox, A. T. Lee, E. Leitch, D. Li, C. Liang, D. Luong-Van, G. Marsden, J. J. McMahon, J. Mehl, S. S. Meyer, L. Mocanu, T. E. Montroy, T. Natoli, J. P. Nibarger, V. Novosad, S. Padin, C. Pryke, C. L. Reichardt, J. E. Ruhl, B. R. Saliwanchik, J. T. Sayre, K. K. Schaffer, B. Schulz, G. Smecher, A. A. Stark, K. T. Story, C. Tucker, K. Vanderlinde, J. D. Vieira, M. P. Viero, G. Wang, V. Yefremenko, O. Zahn, and M. Zemcov, *Detection of B-Mode Polarization in the Cosmic Microwave Background with Data from the South Pole Telescope*, *Physical Review Letters* **111** (Oct., 2013) 141301, [[arXiv:1307.5830](#)].
- [21] V. Acquaviva and C. Baccigalupi, *Dark energy records in lensed cosmic microwave background*, *Phys. Rev. D* **74** (Nov., 2006) 103510, [[astro-ph/0507644](#)].
- [22] K. M. Smith, W. Hu, and M. Kaplinghat, *Cosmological information from lensed CMB power spectra*, *Phys. Rev. D* **74** (Dec., 2006) 123002, [[astro-ph/0607315](#)].
- [23] W. Hu, *Dark energy and matter evolution from lensing tomography*, *Phys. Rev. D* **66** (Oct., 2002) 083515, [[astro-ph/0208093](#)].
- [24] L. E. Bleem, A. van Engelen, G. P. Holder, K. A. Aird, R. Armstrong, M. L. N. Ashby, M. R. Becker, B. A. Benson, T. Biesiadzinski, M. Brodwin, M. T. Busha, J. E. Carlstrom, C. L. Chang, H. M. Cho, T. M. Crawford, A. T. Crites, T. de Haan, S. Desai, M. A. Dobbs, O. Doré, J. Dudley, J. E. Geach, E. M. George, M. D. Gladders, A. H. Gonzalez, N. W. Halverson, N. Harrington, F. W. High, B. P. Holden, W. L. Holzapfel, S. Hoover, J. D. Hrubes, M. Joy, R. Keisler, L. Knox, A. T. Lee, E. M. Leitch, M. Lueker, D. Luong-Van, D. P. Marrone, J. Martinez-Manso, J. J. McMahon, J. Mehl, S. S. Meyer, J. J. Mohr, T. E. Montroy, T. Natoli, S. Padin, T. Plagge, C. Pryke, C. L. Reichardt, A. Rest, J. E. Ruhl, B. R. Saliwanchik, J. T. Sayre, K. K. Schaffer, L. Shaw, E. Shirokoff, H. G. Spieler, B. Stalder, S. A. Stanford, Z. Staniszewski, A. A. Stark, D. Stern, K. Story, A. Vallinotto, K. Vanderlinde, J. D. Vieira, R. H. Wechsler, R. Williamson, and O. Zahn, *A Measurement of the Correlation of*

*Galaxy Surveys with CMB Lensing Convergence Maps from the South Pole Telescope*, *ApJ Letters* **753** (July, 2012) L9, [[arXiv:1203.4808](#)].

- [25] B. D. Sherwin, S. Das, A. Hajian, G. Addison, J. R. Bond, D. Crichton, M. J. Devlin, J. Dunkley, M. B. Gralla, M. Halpern, J. C. Hill, A. D. Hincks, J. P. Hughes, K. Huffenberger, R. Hlozek, A. Kosowsky, T. Louis, T. A. Marriage, D. Marsden, F. Menanteau, K. Moodley, M. D. Niemack, L. A. Page, E. D. Reese, N. Sehgal, J. Sievers, C. Sifón, D. N. Spergel, S. T. Staggs, E. R. Switzer, and E. Wollack, *The Atacama Cosmology Telescope: Cross-correlation of cosmic microwave background lensing and quasars*, *Phys. Rev. D* **86** (Oct., 2012) 083006, [[arXiv:1207.4543](#)].
- [26] N. Hand, A. Leauthaud, S. Das, B. D. Sherwin, G. E. Addison, J. R. Bond, E. Calabrese, A. Charbonnier, M. J. Devlin, J. Dunkley, T. Erben, A. Hajian, M. Halpern, J. Harnois-Déraps, C. Heymans, H. Hildebrandt, A. D. Hincks, J.-P. Kneib, A. Kosowsky, M. Makler, L. Miller, K. Moodley, B. Moraes, M. D. Niemack, L. A. Page, B. Partridge, N. Sehgal, H. Shan, J. L. Sievers, D. N. Spergel, S. T. Staggs, E. R. Switzer, J. E. Taylor, L. Van Waerbeke, and E. J. Wollack, *First Measurement of the Cross-Correlation of CMB Lensing and Galaxy Lensing*, *ArXiv e-prints* (Nov., 2013) [[arXiv:1311.6200](#)].
- [27] P. A. R. Ade, Y. Akiba, A. E. Anthony, K. Arnold, M. Atlas, D. Barron, D. Boettger, J. Borrill, S. Chapman, Y. Chinone, M. Dobbs, T. Elleflot, J. Errard, G. Fabbian, C. Feng, D. Flanagan, A. Gilbert, W. Grainger, N. W. Halverson, M. Hasegawa, K. Hattori, M. Hazumi, W. L. Holzapfel, Y. Hori, J. Howard, P. Hyland, Y. Inoue, G. C. Jaehnig, A. Jaffe, B. Keating, Z. Kermish, R. Keskitalo, T. Kisner, M. Le Jeune, A. T. Lee, E. Linder, E. M. Leitch, M. Lungu, F. Matsuda, T. Matsumura, X. Meng, N. J. Miller, H. Morii, S. Moyerman, M. J. Myers, M. Navaroli, H. Nishino, H. Paar, J. Peloton, E. Quealy, G. Rebeiz, C. L. Reichardt, P. L. Richards, C. Ross, I. Schanning, D. E. Schenck, B. Sherwin, A. Shimizu, C. Shimmin, M. Shimon, P. Siritanasak, G. Smecher, H. Spieler, N. Stebor, B. Steinbach, R. Stompor, A. Suzuki, S. Takakura, T. Tomaru, B. Wilson, A. Yadav, O. Zahn, and Polarbear Collaboration, *Measurement of the Cosmic Microwave Background Polarization Lensing Power Spectrum with the POLARBEAR Experiment*, *Physical Review Letters* **113** (July, 2014) 021301.
- [28] R. Laureijs, J. Amiaux, S. Arduini, J. . Auguères, J. Brinchmann, R. Cole, M. Cropper, C. Dabin, L. Duvet, A. Ealet, and et al., *Euclid Definition Study Report*, *ArXiv e-prints* (Oct., 2011) [[arXiv:1110.3193](#)].
- [29] L. Amendola, S. Appleby, D. Bacon, T. Baker, M. Baldi, N. Bartolo, A. Blanchard, C. Bonvin, S. Borgani, E. Branchini, C. Burrage, S. Camera, C. Carbone, L. Casarini, M. Cropper, C. de Rham, C. Di Porto, A. Ealet, P. G. Ferreira, F. Finelli, J. García-Bellido, T. Giannantonio, L. Guzzo, A. Heavens, L. Heisenberg, C. Heymans, H. Hoekstra, L. Hollenstein, R. Holmes, O. Horst, K. Jahnke, T. D. Kitching, T. Koivisto, M. Kunz, G. La Vacca, M. March, E. Majerotto, K. Markovic, D. Marsh, F. Marulli, R. Massey, Y. Mellier, D. F. Mota, N. Nunes, W. Percival, V. Pettorino, C. Porciani, C. Quercellini, J. Read, M. Rinaldi, D. Sapone, R. Scaramella, C. Skordis, F. Simpson, A. Taylor, S. Thomas, R. Trotta, L. Verde, F. Vernizzi, A. Vollmer, Y. Wang, J. Weller, and T. Zlosnik, *Cosmology and Fundamental Physics with the Euclid Satellite*, *Living Reviews in Relativity* **16** (Sept., 2013) 6, [[arXiv:1206.1225](#)].
- [30] R. Pearson and O. Zahn, *Cosmology from cross correlation of CMB lensing and galaxy surveys*, *Phys. Rev. D* **89** (Feb., 2014) 043516, [[arXiv:1311.0905](#)].
- [31] M. Killedar, P. D. Lasky, G. F. Lewis, and C. J. Fluke, *Gravitational lensing with three-dimensional ray tracing*, *MNRAS* **420** (Feb., 2012) 155–169, [[arXiv:1110.4894](#)].
- [32] S. Hilbert, R. B. Metcalf, and S. D. M. White, *Imaging the cosmic matter distribution using gravitational lensing of pre-galactic HI*, *MNRAS* **382** (Dec., 2007) 1494–1502, [[arXiv:0706.0849](#)].
- [33] H. M. P. Couchman, A. J. Barber, and P. A. Thomas, *Measuring the three-dimensional shear*

- from simulation data, with applications to weak gravitational lensing, *MNRAS* **308** (Sept., 1999) 180–200, [[astro-ph/9810063](#)].
- [34] C. Carbone, C. Baccigalupi, M. Bartelmann, S. Matarrese, and V. Springel, *Lensed CMB temperature and polarization maps from the Millennium Simulation*, *MNRAS* **396** (June, 2009) 668–679, [[arXiv:0810.4145](#)].
  - [35] C. Carbone, M. Baldi, V. Pettorino, and C. Baccigalupi, *Maps of CMB lensing deflection from N-body simulations in Coupled Dark Energy Cosmologies*, *JCAP* **9** (Sept., 2013) 4, [[arXiv:1305.0829](#)].
  - [36] C. Antolini, Y. Fantaye, M. Martinelli, C. Carbone, and C. Baccigalupi, *N-body lensed CMB maps: lensing extraction and characterization*, *JCAP* **2** (Feb., 2014) 39, [[arXiv:1311.7112](#)].
  - [37] W. Hu and T. Okamoto, *Mass Reconstruction with Cosmic Microwave Background Polarization*, *ApJ* **574** (Aug., 2002) 566–574, [[astro-ph/0111606](#)].
  - [38] R. Blandford and R. Narayan, *Fermat’s principle, caustics, and the classification of gravitational lens images*, *ApJ* **310** (Nov., 1986) 568–582.
  - [39] B. Jain, U. Seljak, and S. White, *Ray-tracing Simulations of Weak Lensing by Large-Scale Structure*, *ApJ* **530** (Feb., 2000) 547–577, [[astro-ph/9901191](#)].
  - [40] F. Pace, M. Maturi, M. Meneghetti, M. Bartelmann, L. Moscardini, and K. Dolag, *Testing the reliability of weak lensing cluster detections*, *A&A* **471** (Sept., 2007) 731–742, [[astro-ph/0702031](#)].
  - [41] S. Hilbert, J. Hartlap, S. D. M. White, and P. Schneider, *Ray-tracing through the Millennium Simulation: Born corrections and lens-lens coupling in cosmic shear and galaxy-galaxy lensing*, *A&A* **499** (May, 2009) 31–43, [[arXiv:0809.5035](#)].
  - [42] M. R. Becker, *CALCLENS: weak lensing simulations for large-area sky surveys and second-order effects in cosmic shear power spectra*, *MNRAS* **435** (Oct., 2013) 115–132.
  - [43] S. Das and P. Bode, *A Large Sky Simulation of the Gravitational Lensing of the Cosmic Microwave Background*, *ApJ* **682** (July, 2008) 1–13, [[arXiv:0711.3793](#)].
  - [44] P. Fosalba, E. Gaztañaga, F. J. Castander, and M. Manera, *The onion universe: all sky lightcone simulations in spherical shells*, *MNRAS* **391** (Nov., 2008) 435–446, [[arXiv:0711.1540](#)].
  - [45] M. Bartelmann, *TOPICAL REVIEW Gravitational lensing*, *Classical and Quantum Gravity* **27** (Dec., 2010) 233001, [[arXiv:1010.3829](#)].
  - [46] C. Vale and M. White, *Simulating Weak Lensing by Large-Scale Structure*, *ApJ* **592** (Aug., 2003) 699–709, [[astro-ph/0303555](#)].
  - [47] B. Li, L. J. King, G.-B. Zhao, and H. Zhao, *An analytic ray-tracing algorithm for weak lensing*, *MNRAS* **415** (July, 2011) 881–892, [[arXiv:1012.1625](#)].
  - [48] W. Hu, *Weak lensing of the CMB: A harmonic approach*, *Phys. Rev. D* **62** (Aug., 2000) 043007, [[astro-ph/0001303](#)].
  - [49] M. Baldi, *The CoDECS project: a publicly available suite of cosmological N-body simulations for interacting dark energy models*, *MNRAS* **422** (May, 2012) 1028–1044, [[arXiv:1109.5695](#)].
  - [50] C. Carbone, V. Springel, C. Baccigalupi, M. Bartelmann, and S. Matarrese, *Full-sky maps for gravitational lensing of the cosmic microwave background*, *MNRAS* **388** (Aug., 2008) 1618–1626, [[arXiv:0711.2655](#)].
  - [51] V. Springel, M. White, and L. Hernquist, *Hydrodynamic Simulations of the Sunyaev-Zeldovich Effect(s)*, *ApJ* **549** (Mar., 2001) 681–687, [[astro-ph/0008133](#)].
  - [52] W. A. Watson, J. M. Diego, S. Gottlöber, I. T. Iliev, A. Knebe, E. Martínez-González, G. Yepes, R. B. Barreiro, J. González-Nuevo, S. Hotchkiss, A. Marcos-Caballero, S. Nadathur,

- and P. Vielva, *The Jubilee ISW project - I. Simulated ISW and weak lensing maps and initial power spectra results*, *MNRAS* **438** (Feb., 2014) 412–425, [[arXiv:1307.1712](#)].
- [53] A. Lewis, *Lensed CMB simulation and parameter estimation*, *Phys. Rev. D* **71** (Apr., 2005) 083008, [[astro-ph/0502469](#)].
  - [54] G. Fabbian and R. Stompor, *High-precision simulations of the weak lensing effect on cosmic microwave background polarization*, *A&A* **556** (Aug., 2013) A109, [[arXiv:1303.6550](#)].
  - [55] I. Kayo, A. Taruya, and Y. Suto, *Probability Distribution Function of Cosmological Density Fluctuations from a Gaussian Initial Condition: Comparison of One-Point and Two-Point Lognormal Model Predictions with N-Body Simulations*, *ApJ* **561** (Nov., 2001) 22–34, [[astro-ph/0105218](#)].
  - [56] A. Taruya, M. Takada, T. Hamana, I. Kayo, and T. Futamase, *Lognormal Property of Weak-Lensing Fields*, *ApJ* **571** (June, 2002) 638–653, [[astro-ph/0202090](#)].
  - [57] R. Takahashi, M. Sato, T. Nishimichi, A. Taruya, and M. Oguri, *Revising the Halofit Model for the Nonlinear Matter Power Spectrum*, *ApJ* **761** (Dec., 2012) 152, [[arXiv:1208.2701](#)].
  - [58] R. E. Smith, J. A. Peacock, A. Jenkins, S. D. M. White, C. S. Frenk, F. R. Pearce, P. A. Thomas, G. Efstathiou, and H. M. P. Couchman, *Stable clustering, the halo model and non-linear cosmological power spectra*, *MNRAS* **341** (June, 2003) 1311–1332, [[astro-ph/0207664](#)].
  - [59] A. Benoit-Lévy, K. M. Smith, and W. Hu, *Non-Gaussian structure of the lensed CMB power spectra covariance matrix*, *Phys. Rev. D* **86** (Dec., 2012) 123008, [[arXiv:1205.0474](#)].
  - [60] K. M. Smith, W. Hu, and M. Kaplinghat, *Weak lensing of the CMB: Sampling errors on B modes*, *Phys. Rev. D* **70** (Aug., 2004) 043002, [[astro-ph/0402442](#)].